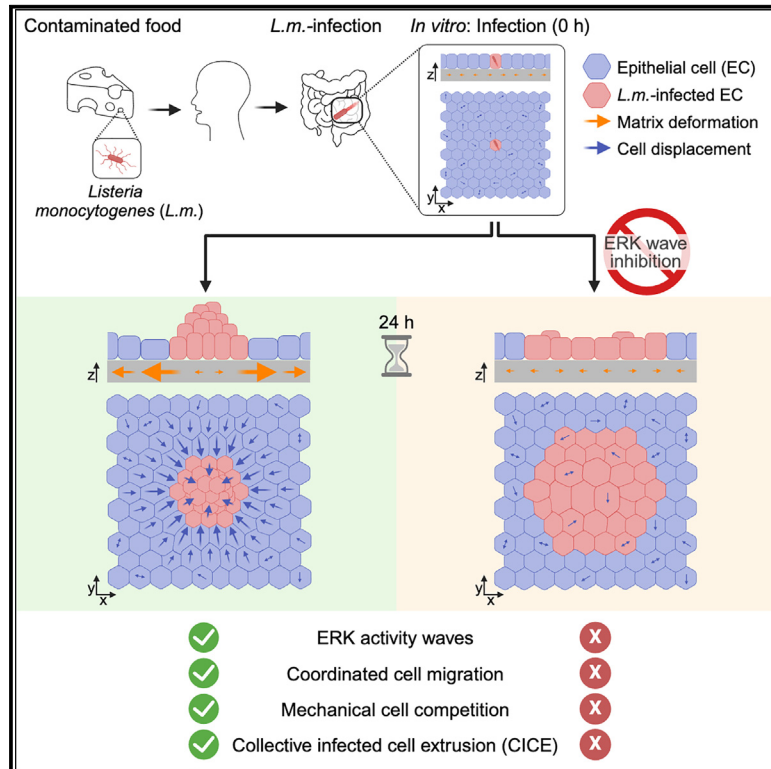**Article**

ERK activation waves coordinate mechanical cell competition leading to collective elimination via extrusion of bacterially infected cells

Graphical abstract

Authors

Lara Hundsdorfer, Marie Muenkel, Raul Aparicio-Yuste, ..., Boris Maček, Serge Mostowy, Effie E. Bastounis

Correspondence

effie.bastounis@uni-tuebingen.de

In brief

Collective infected cell extrusion (CICE) enables uninfected epithelial cells to eliminate adjacent infected cells and limit infection spread. Hundsdorfer et al. show that during infection with the intracellular bacterium *Listeria monocytogenes*, CICE depends on the propagation of ERK waves across the epithelium monolayer, triggering key changes in host cell biomechanics.

Highlights

- Increased frequency ERK waves travel between epithelial cells during infection

- ERK waves enable surrounder cells to polarize and reinforce monolayer stresses

- Epithelial cells' altered mechanics drive collective infected cell extrusion (CICE)

- In the absence of ERK waves, CICE is diminished and bacterial spread is enhanced

CellPress

Article

ERK activation waves coordinate mechanical cell competition leading to collective elimination via extrusion of bacterially infected cells

Lara Hundsdorfer,[1,2] Marie Muenkel,[1,2] Raul Aparicio-Yuste,[3] Julio Cesar Sanchez-Rendon,[1,2] Maria Jose Gomez-Benito,[3] Aylin Balmes,[4] Tilman E. Schäffer,[4] Ana Velic,[5] Yi-Ting Yeh,[6] Iordania Constantinou,[7,8] Kathryn Wright,[9] Gizem Özbaykal Güler,[9] Dominik Brokatzky,[9] Boris Maček,[5] Serge Mostowy,[9] and Effie E. Bastounis[1,2,10,*]

[1]Interfaculty Institute of Microbiology and Infection Medicine, University of Tübingen, 72076 Tübingen, Baden-Württemberg, Germany
[2]Cluster of Excellence EXC 2124 Controlling Microbes to Fight Infections, University of Tübingen, 72076 Tübingen, Baden-Württemberg, Germany
[3]Engineering Research Institute of Aragon (I3A), Department of Mechanical Engineering, University of Zaragoza, 50018 Zaragoza, Aragon, Spain
[4]Institute of Applied Physics, University of Tübingen, 72076 Tübingen, Baden-Württemberg, Germany
[5]Proteome Center Tübingen, University of Tübingen, 72076 Tübingen, Baden-Württemberg, Germany
[6]Department of Mechanical Engineering, University of Washington, Seattle, WA 98195, USA
[7]Institute of Microtechnology, Technische Universität Brauschweig, 38106 Braunschweig, Lower Saxony, Germany
[8]Center of Pharmaceutical Engineering (PVZ), Technische Universität Braunschweig, 38106 Braunschweig, Lower Saxony, Germany
[9]Department of Infection Biology, London School of Hygiene and Tropical Medicine, London WC1E 7HT, UK
[10]Lead contact
*Correspondence: effie.bastounis@uni-tuebingen.de
https://doi.org/10.1016/j.celrep.2024.115193

SUMMARY

Epithelial cells respond to infection with the intracellular bacterial pathogen *Listeria monocytogenes* by altering their mechanics to promote collective infected cell extrusion (CICE) and limit infection spread across cell monolayers. However, the underlying biochemical pathways remain elusive. Here, using *in vitro* (epithelial monolayers) and *in vivo* (zebrafish larvae) models of infection with *L. monocytogenes* or *Shigella flexneri*, we explored the role of extracellular-signal-regulated kinase (ERK) activity waves in coordinating the mechanical battle between infected and surrounder uninfected cells that leads to CICE. We discovered that when ERK waves are suppressed, cells fail to exhibit alterations in cell shape and kinematics associated with CICE and behave more like quiescent uninfected monolayers. In particular, uninfected cells surrounding infection foci are unable to polarize, reinforce their monolayer stresses, and promote CICE. Our findings reveal that crosstalk between ERK waves and cell mechanics is key to collective elimination of large domains of infected cells.

INTRODUCTION

The food-borne facultative intracellular bacterial pathogen *Listeria monocytogenes* (*L.m.*), like other bacterial and viral pathogens, can non-lytically spread from cell to cell by triggering rapid assembly of host cell actin filaments at one bacterial pole, forming "actin comet tails."[1,2] Similar but distinct strategies are employed by other bacterial pathogens like tick-borne *Rickettsia parkeri* (*R.p.*) and enteropathogenic *Shigella flexneri* (*S.f.*).[3,4] After initial invasion of a single epithelial cell, pathogens employing actin-based motility replicate and spread to neighboring cells, leading to formation of large domains of infected cells (infection foci) comprising hundreds of cells.[5] In response, host cells alter their biomechanics to counteract bacterial spread.[4,6,7] For example, when epithelial cells in monolayer are infected with low doses of *L.m.*, a mechanical battle takes place, whereby stiffer and more

contractile uninfected surrounder cells (surrounders) collectively move toward domains of infected cells, squeezing them and promoting collective infected cell extrusion (CICE), ultimately leading to infected cell death.[8]

CICE depends on alterations in cell contractility, cell stiffness, and intercellular adhesions between infected and surrounder uninfected cells, but little is known about the interplay between cell mechanics and biochemical signaling during this process.[8] A role for NF-κB signaling is supported by evidence that CICE occurs only in epithelia infected with a *Rickettsia* mutant strain that fails to inactivate NF-κB.[8,9] Nevertheless, NF-κB inhibition only partially reduces CICE (25%), suggesting that additional pathways are involved.[8] This hypothesis is further supported by the upregulation of markers associated with epithelial-to-mesenchymal transition (EMT) in both infected and surrounder cells and biochemical and biomechanical changes that are reminiscent

of EMT.[8] Besides NF-κB, also the extracellular-signal-regulated kinase (ERK) plays a role in this process.[10,11] However, whether ERK is involved in the mechanical cell competition driving CICE remains unclear. Seemingly poorly understood is how NF-κB and ERK signaling pathways spatiotemporally interact with host cell biomechanics to regulate CICE and limit infection spread.

In recent years, the ERK pathway has drawn attention and has been characterized as a fast and modular mechanosensitive pathway involved in many processes ranging from wound healing to development and innate immune responses.[12–15] ERK signaling can oscillate autonomously within single cells, modulating their behavior based on internal cues.[16] Additionally, ERK signals can propagate as waves across neighboring cells, coordinating tissue-wide responses.[17,18] This dual mode of ERK activation—both within individual cells and across cell communities—provides a highly adaptable mechanism for cell organization and long-range intercellular communication at orders of magnitude faster than diffusion alone would allow.[18–20] The frequency and amplitude of ERK waves may vary depending on the external stimulus, leading to transient or sustained ERK activation, which in turn results in different cell fates (e.g., differentiation versus proliferation).[21,22] Cytokines and pro-inflammatory ligands also modulate frequency and amplitude of ERK waves, suggesting that changes in ERK dynamics could occur during infection.[23,24] However, despite extensive research in other biological contexts,[18,25,26] the role of ERK waves in facilitating rapid information transmission between epithelial cell monolayers during infection has not been investigated to date.

Based on this, and evidence implicating ERK waves in collective extrusion of UV-treated cells[27] and apoptotic cells,[28] we speculated that ERK waves could regulate fast collective migration of surrounder cells toward infection foci (the driving force behind CICE). Monitoring ERK activity dynamics across epithelial monolayers infected with *L.m.* or *S.f.*, we found that ERK activity waves coordinate alterations in host cell shapes, kinematics, and dynamics that occur during infection and are key in driving CICE. Importantly, ERK is key to CICE also in *S.f.*-infected zebrafish larvae. Our findings highlight ERK waves as a spatial alarm signal propagating across monolayers to modulate cell biomechanics, thus enabling fast coordinated action against the threat of infection spread.

RESULTS

ERK is activated by EGFR signaling during epithelial cell infection with *L.m.* and is important for CICE

To determine whether ERK signaling is altered during *L.m.* infection of epithelial cells, we infected Madin-Darby Canine Kidney (MDCK) epithelial cells with *L.m.* for 24 h until CICE occurrence.[8] Western blot analysis revealed that the levels of the two ERK isoforms ERK1 and ERK2 (ERK1/2) remained constant during infection, while phosphorylated ERK1/2 (*p*-ERK1/2), a proxy for ERK activation, increased in infected compared to uninfected cells (Figures 1A and 1B). Consistently, the levels of auto-phosphorylated EGFR and phosphorylated MEK1/2 were significantly higher in infected than in uninfected cells (Figures 1A and 1B). These findings demonstrate that *L.m.* infection activates EGFR and its downstream signaling kinases, MEK1/2 and ERK1/2.

Next, to determine whether ERK is involved in CICE, we treated infected MDCK cells with a MEK inhibitor (PD0325901) to inhibit ERK activation (Figure S1A). Under these conditions, CICE was suppressed, with mound volume decreasing by 60% compared to control samples (Figures 1C and 1D), and infected cells and their nuclei appeared no longer squeezed but regularly organized (Figures 1C and S1B). Treatment with an EGFR inhibitor (PD153035) similarly reduced mound volume by 70% (Figures S1C and S1D). Consistent with our previous findings, reduced mound volume was associated with an increase in infection foci area and bacterial load (Figures 1E and 1F; Video S1).

To explore whether ERK inhibition affects pathways related to the cytoskeleton, contractility, and cell adhesion—essential for CICE—we performed phosphoproteomics followed by Gene Ontology (GO) analysis.[29] While uninfected samples treated with MEK inhibitor displayed only a few differentially phosphorylated proteins compared to untreated/uninfected samples (Figures 1H, S1E and S1F), in infected samples, MEK inhibition led to a significant increase in differentially phosphorylated proteins (Figure 1H). Notably, multiple GO terms related to cell contractility and cell-cell or cell-ECM adhesion were differentially regulated in infected samples, at both 8 and 24 hours post-infection (hpi) (see magenta-labeled in Figure 1I). These findings suggested a link between ERK activation and cell biomechanics (e.g., contractility, motility) during infection, which we further explored.

ERK inhibition prevents the polarization and collective alignment of uninfected surrounder cells and the squeezing of infected cells

Infected cells and their uninfected surrounders undergo distinct changes in shape that are crucial for CICE.[8] To determine whether ERK inhibition affects cell shape, we first analyzed shape descriptors in uninfected monolayers. Both ERK-inhibited and control MDCK cells formed regularly packed polygons with random orientation, although in ERK-inhibited samples radial alignment was even lower than in controls (Figure S2A). However, there were no significant differences in mean cell area, aspect ratio, radial alignment, or shape factor q (cell perimeter to square root of area)[30] between the two conditions (Figure S2B), ruling out ERK may impact cell shape.

By contrast, ERK inhibition significantly altered the shape of cells in *L.m.*-infected monolayers: infected cells appeared enlarged rather than squeezed, while surrounder cells failed to polarize and looked like cells in non-infected wells (Figures 2A–2C). Additionally, surrounder cells failed to align their long axes with neighboring cells, lacking the nematic order observed in control infected monolayers (Figures 2D and 2E). Also, no increase in shape factor q, a measure of tissue fluidity, was observed in uninfected surrounders upon MEK inhibition (Figures 2F and S2B). This suggests that ERK inhibition disrupts polarization, nematic ordering, and tissue fluidity necessary for surrounder cells to collectively take action and squeeze infected cells.

ERK inhibition abrogates increases in host cell speed and migration coordination during *L.m.* infection

To determine whether ERK inhibition affects cell motility during infection, we tracked MDCK cells infected with a low dose of
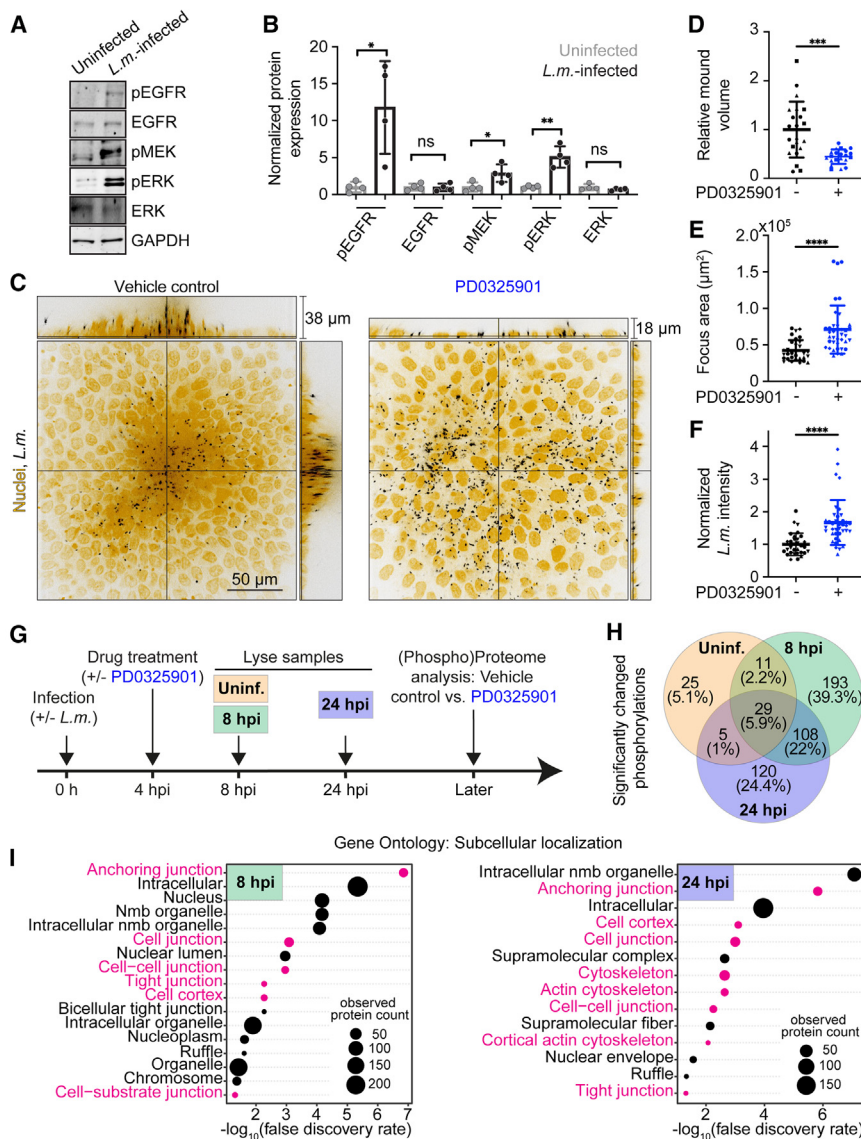
Figure 1. ERK activation increases in host cells during *L.m.* infection and is required for mound formation

(A) Representative cropped western blots from lysates of uninfected and *L.m.*-infected MDCK cell monolayers at 24 hpi. Total or phosphorylated levels (p) of the indicated proteins were probed for pEGFR, EGFR, pMEK, pERK, ERK, and GAPDH.

(B) Bar plots of relative expression of proteins probed in (A). Measurements normalized to GAPDH expression of each condition and expressed as fold change relative to mean uninfected cells' expression level. Lines: mean ± SD, unpaired t test: *$p < 0.05$, **$p < 0.01$.

(C) Orthogonal views of *L.m.*-infected MDCK cells at 24 hpi treated with vehicle control (left) or 50 μM PD0325901 (right) at 4 hpi. Host nuclei: yellow; *L.m.*: black.

(D–F) Quantification of *L.m.* infection focus properties of the conditions shown in (C): (D) relative mound volume, (E) focus area (μm²), (F) relative *L.m.* fluorescence intensity. D, F normalized to mean of control cells. Lines: mean ± SD, WRST: ***$p < 0.001$, ****$p < 0.0001$; different shapes indicate data from $N = 3$ independent experiments.

(G) Sketch of phosphoproteomics experimental setup. Uninfected samples (orange) or *L.m.*-infected samples at 8 (green) and 24 (blue) hpi treated with vehicle control or PD0325901 are compared.

(H) Venn diagram displaying the number and percentage of significantly changed protein phosphorylation levels comparing control to PD0325901-treated cell samples as explained in (G).

(I) Functional enrichment analysis of differentially phosphorylated proteins of samples shown in (G), displaying in bubble plots the GO cellular components significantly altered between control versus PD0325901-treated samples. Cell-mechanics-related GO components are in magenta. Left: *L.m.*-infected for 8 h, right: *L.m.*-infected for 24 h. See also Figure S1, Video S1, and Table S1.

L.m., treated or not with MEK inhibitor. We started live-cell imaging at around 6 hpi and centered the imaged field of view around a given infection focus to also monitor its growth (Figures 3A, 3B, S3A, and S3B; Video S2). To ensure imaging of intracellular bacteria only, we used an *L.m.* strain expressing mtagRFP under the ActA promoter control,[31] which is active when *L.m.* enters the host cell cytosol, and maintained the cells in gentamicin-containing medium to eliminate extracellular bacteria and prevent further host cell invasion events.[32] We also imaged control uninfected cells under same conditions. Using particle image velocimetry (PIV) on the cell nuclei images, we calculated cell displacements over time (Figures 3A, 3B, S3C, and S3D; Video S2). The average migration speed of uninfected monolayers was 4 μm/h, consistent with previous studies and reflecting the quiescent state of these confluent cells (Figures 3C and S3E). ERK inhibition did not significantly affect uninfected cells' migration speed, although this was consistently lower than in controls.

Thus, ERK has only a modest impact on cell movement in dense, confluent cell monolayers, possibly related to the mild reduction in collective cell alignment (Figures S2A and S3C–S3F).

In contrast, *L.m.*-infected cell monolayers showed a quasi-linear increase in migration speed, starting 14 hpi and peaking at 25 hpi (Figures 3A and 3C). The correlation length of movement, a measure of how far the motion of individual cells remains correlated to each other, also increased, highlighting the collective response of surrounder cells migrating toward the infection focus (Figures 3D and S3F). Accordingly, displacement vector maps showed that surrounder cells collectively moved toward the infection focus (Figure 3A), as highlighted in the rose plots (Figures 3E and 3F). However, ERK-inhibited infected monolayers exhibited no increase in migration speed and correlation length over time post-infection (Figures 3B–3D, and 3G), indicating that upon ERK inhibition, cells in infected monolayers behave like those in non-infected samples.
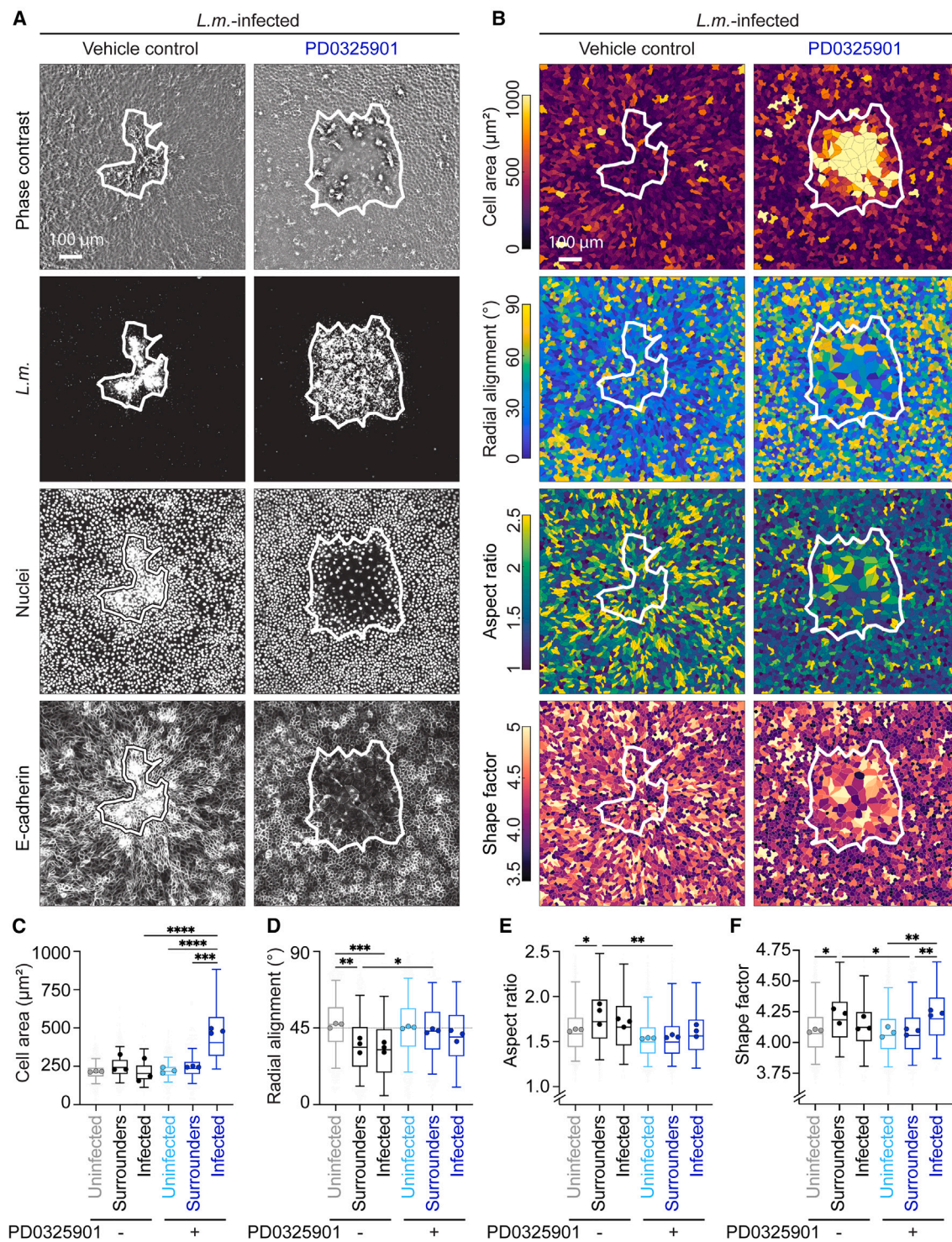
Figure 2. ERK inhibition abrogates collective alignment of surrounder cells and alters the shape of infected cells

(A) *L.m.*-infected MDCK cells at 24 hpi, treated at 4 hpi with vehicle control (1st column) or 50 μM PD0325901 (2nd column). Rows: phase contrast, *L.m.*, cell nuclei, E-cadherin fluorescence. White outline: infection focus contour.

(B) Same images as in (A) with cells in rows color-coded for: cell area (μm²), radial alignment (°) of major cell axis, cell aspect ratio, shape factor (see STAR Methods).

(legend continued on next page)

Infection induces dynamic ERK activation waves that travel between neighboring cells and are essential for CICE

The lack of coordinated cell migration in *L.m.*-infected, ERK-inhibited samples suggested that ERK activation waves might drive these behavioral changes. To test this, we treated cells with phorbol-12-myristate-13-acetate (PMA), which acutely and constitutively activates ERK,[20,33] thus abrogating ERK activation waves. Under these conditions, the volume of infection mounds was significantly diminished (Figures S4A and S4B), and cells showed random migration, similar to ERK-inhibited cells, lacking the directional movement seen in untreated cells (Figure S4C). Conversely, treatment with epidermal growth factor (EGF), which was previously shown to increase single-cell ERK activity pulses and wave frequency occurrence,[15,23] led to faster formation of mounds and thus significantly smaller infection foci than untreated infected samples, although the precise factors driving accelerated CICE were not investigated further (Figures S4B and S4D). Collectively, these findings suggest that ERK waves, and not constitutive ERK activity, are crucial for the directional migration of surrounder cells toward the infection focus and subsequent CICE.

To examine the spatiotemporal modulation of ERK activation during infection, we performed Förster resonance energy transfer (FRET) imaging on EKARE-NLS-expressing MDCK cells and measured the increase in the FRET/CFP ratio in the cells' nuclei as proxy for ERK activation.[15,34] In absence of infection, the frequency of ERK waves propagating from one cell to neighboring cells in densely packed MDCK cell monolayers was low. This is consistent with previous findings suggesting that when monolayer cell density is increased, basal ERK activity and frequency of waves are diminished (Figures S4E and S4F; Video S3).[16] Moreover, when cells were treated with MEK inhibitor, ERK activity levels were decreased, and waves were completely abolished (Video S3). In contrast, when cells were infected with *L.m.*, we observed a significant increase in the frequency of ERK waves propagating through the monolayer, seemingly traveling along both infected and surrounder cells (Figure 4A; Video S3). To better quantify single-cell ERK activity and wave propagation, we first constructed kymographs by considering the infection focus center as the center of the new polar coordinate system and averaging ERK activity radially while plotting it over time (Figures S4F and S4G). We also constructed kymographs by following individual cells ordered based on the distance from the focus center (or field of view center for uninfected cells) and plotted their mean ERK activity over time (Figures 4B and 4C). In both cases, the baseline ERK activity in single cells of infected monolayers was increased as compared to non-infected samples but decreased over time as confluence increased, similar to uninfected samples (Figures 4B, S4F and S4G). Median ERK activity was considerably lower in ERK-inhibited (with MEK inhibitor) samples and higher in activated (with PMA) samples, irrespective of whether they were infected or not. Moreover, cells

displayed neither single-cell oscillations in ERK activity (see median single-cell ERK activity in Figure 4B) nor waves (Video S3). To ensure that cells did not photobleach, we performed FRET recordings every 1 h instead of every 10 min in some wells, but even under these imaging conditions, ERK activity decreased over time (Video S3).

Using the ARCOS algorithm to analyze ERK waves from 8 to 16 hpi, we found that ERK wave frequency was significantly higher in infected than in non-infected cell samples (Figures 4D and S4H).[19] However, the size of ERK-activated cell clusters did not significantly differ in infected compared to non-infected cell samples (Figure 4E).[19] At around 14–16 hpi, when extrusion starts, we did not observe clear radial ERK waves traveling away from the infection focus, consistent with these cells not being apoptotic.[8,28] Nevertheless, cell displacement vectors and spontaneous ERK waves suggested a connection between the two processes, consistent with previous findings from non-infectious contexts (Figure 4A).[15] To investigate whether the increase in ERK waves during infection is a global phenomenon, we performed additional FRET imaging on an expanded field of view imaged to capture surrounder cells up to 700 μm away from the infection focus center. Under these conditions, we observed no reduction in ERK activity or the frequency of ERK-activated cell clusters with increasing distance from the infection site, suggesting a global regulation of ERK waves rather than a strictly local effect (Video S3 and Figure S4I). Moreover, upon inhibition (marimastat) of matrix metalloproteases (MMPs),[15] previously involved in ERK wave propagation, we observed a slight decrease in ERK activation waves during infection and suppression of CICE, resulting in larger infection foci than controls (Figures S4J and S4K). These observations suggest that MMPs also contribute to ERK wave dynamics and thus to CICE. Overall, we provide evidence for that a global increase in baseline ERK activity and ERK waves is crucial for the alterations in cell kinematics that occur during infection, and lead to CICE.

Simulations predict that the inability of proximal surrounders to increase their monolayer stresses may be responsible for the lack of CICE in ERK-inhibited infected cells

Since absence of ERK waves suppresses cell morphology and kinematics' alterations arising during L.m. infection, it is likely surrounder and infected cells fail to engage in effective mechanical competition.[8] To test this and determine the mechanical parameters that lead to CICE suppression, we employed a hybrid computational approach, combining agent-based and finite element models. This model simulates epithelial monolayer dynamics, accounting for infection spread by considering the increasing number of infected cells over time (Figure S5). We assumed that surrounder cells can vary their degree of protrusion based on our findings that ERK inhibition reduces polarization of surrounder cells and migration speed (Figure 5A left). We

---

(C–F) Box plots of cell area (C), radial alignment (D), cell aspect ratio (E), shape factor (F) of cells originating from uninfected wells, uninfected surrounders and infected cells treated with vehicle control (grayscale) or 50 μM PD0325901 (bluescale). $N = 4908 \pm 778$ single cells were analyzed per condition. Dots show mean of each of $N = 3$ independent replicates; ANOVA followed by Tukey's multiple comparisons test: $*p < 0.05$, $**p < 0.01$, $***p < 0.001$, $****p < 0.0001$. See also Figure S2.
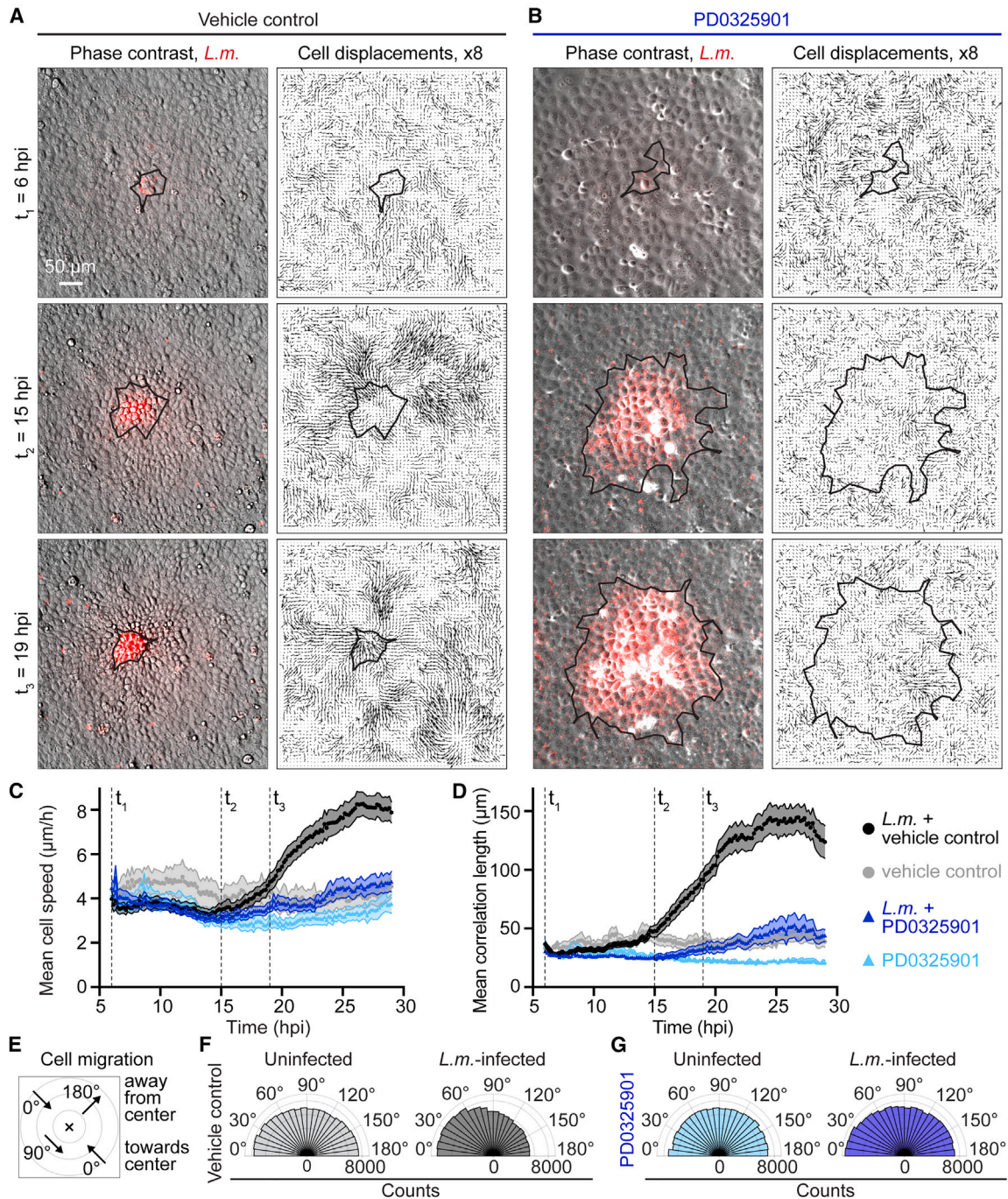
Figure 3. ERK inhibition stalls the increase in cell speed and coordinated migration of MDCK cells during *L.m.* infection

(A and B) Representative video microscopy images of *L.m.*-infected MDCK cell monolayers treated with vehicle control (A) or 50 μM PD0325901 (B) at three indicated time points (rows). Columns: overlay of phase-contrast image with *L.m.* fluorescence, cell displacements (arrows, scaled 8x). Black outline: infection focus contour.

(C and D) Mean cell speed (μm/h, C) and correlation length (μm, D) over time (hpi) shown for uninfected or *L.m.*-infected cells treated or not at 4 hpi with 50 μM PD0325901 (see color legend). Solid line: mean, shaded area: SEM for three independent experiments, $N = 7$ and $N = 18$ recordings for uninfected and *L.m.*-infected conditions, respectively. Dashed lines indicate representative time points shown in (A-B).

(E) Sketch of cell migration directionality angles quantified in (F-G). 0° and 180° correspond to cells moving toward or away from the center of the infection focus (or field of view for uninfected cells), respectively.

(F and G) Rose plots showing cell displacement directionality angle (angle between radial direction and cell displacement, see STAR Methods) for uninfected (left) or *L.m.*-infected cells in monolayer (right), treated with vehicle control (F) or 50 μM PD0325901 (G). See also Figure S3 and Video S2.
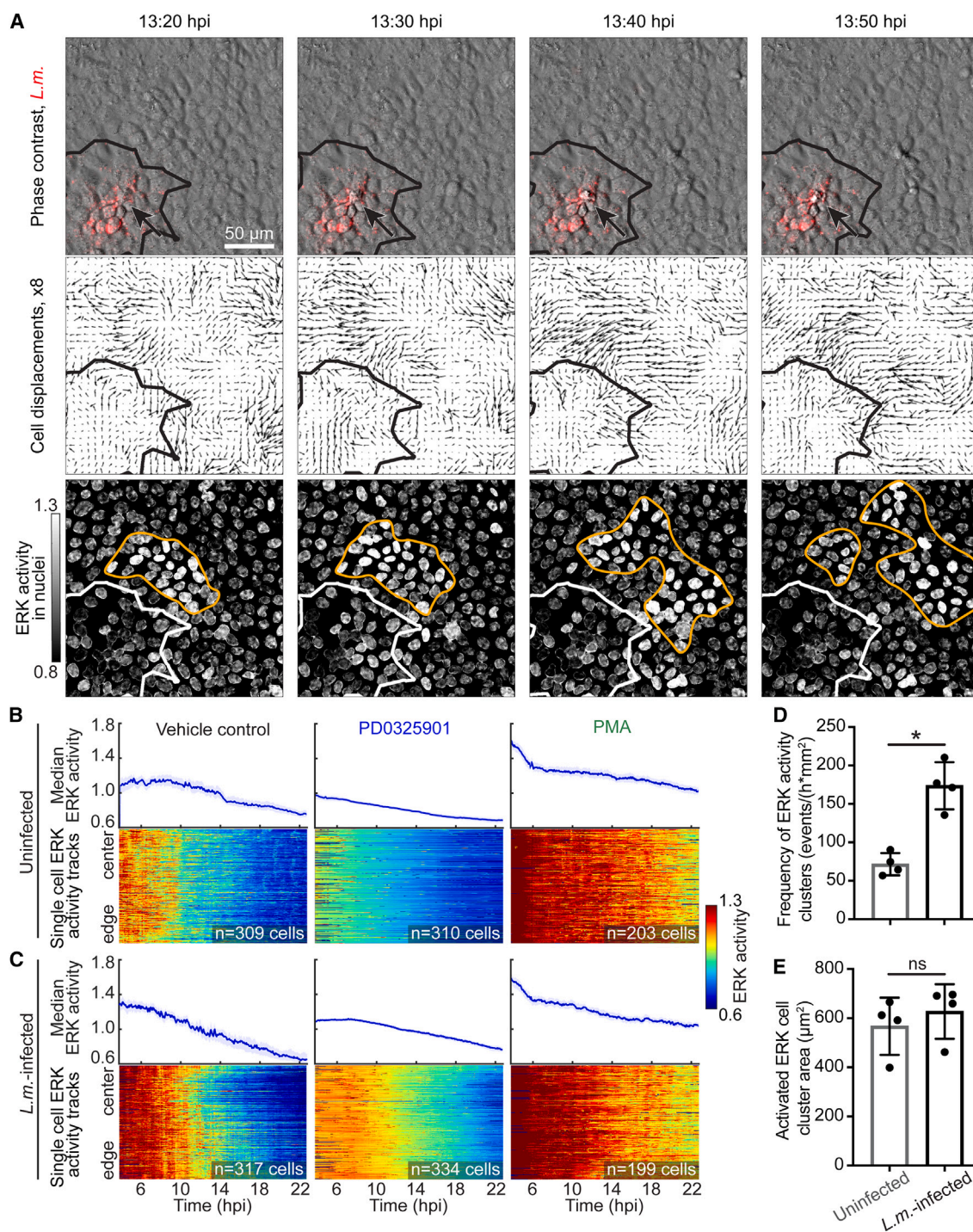
Figure 4. ERK inhibition or constitutive activation abolishes ERK activation waves traveling between MDCK cells during *L.m.* infection

(A) Representative time-lapse images (columns) of *L.m.*-infected MDCK cells monolayers when extrusion of infected cells first occurs. Rows: overlay of phase contrast and *L.m.* fluorescence (red), cell displacements (arrows, scaled 8x), ERK activity in cell nuclei with orange outline indicating ERK activity wave. Black/white outlines: infection focus contour. Arrows point on first extruded infected cell.

(legend continued on next page)

also assumed that contractility and stiffness of infected cells can vary compared to surrounders (Figure 5A middle and right).[8]

We simulated four different cases (Figure 5; Video S4). In case 1, infected cells exhibit lower stiffness (250 Pa) than surrounder cells (500 Pa), leading to polarization of surrounders toward the infection focus because they protrude toward the site of minimum stress, the focus[8] (Figure 5B). As a result, monolayer stresses of uninfected cells surrounding the focus (proximal surrounder) increase, leading to squeezing of infected cells, a prerequisite for CICE. In case 2, we simulated *in vitro* ERK wave inhibition by reducing the surrounder cell force (F^s) so that surrounder cells cannot polarize effectively toward the focus, resulting in loss of infected cell squeezing and reduction of monolayer stresses in proximal surrounders compared to case 1 (Figure 5B). In case 3, we simulated case 2 but also assumed that infected cells have the same stiffness as surrounders (500 Pa). This makes surrounders less competent in squeezing infected cells compared to case 2 (Figure 5B). As in case 2, monolayer stresses of proximal surrounder cells fail to increase. Finally, in case 4, we simulated case 2 but also assumed reduced contractility of infected compared to surrounder cells. As a result, instead of being squeezed, infected cells increase their area (Figure 5B). Similar to cases 2 and 3, monolayer stresses of proximal surrounder cells are weakened.

To summarize, our model predicts that impairing surrounder cell polarization (cases 2–4 versus 1) reduces infected cell squeezing and monolayer stresses reinforcement. Additionally, eliminating stiffness differences between surrounder versus infected cells (case 3 versus 2) further decreases squeezing, albeit slightly. Only when both surrounder cell force and infected cell contractility are reduced (case 4), infected cells enlarge rather than being squeezed.

ERK inhibition deescalates the mechanical competition between infected and surrounder uninfected cells

The model suggested that for infected cell squeezing and CICE to stall (as observed when ERK waves are abrogated), the reinforcement of monolayer stress in surrounder cells must disappear. Additionally, a further reduction in contractility of infected cells may result in cell enlargement rather than squeezing. To confirm these findings *in vitro*, we first performed TFM to measure traction stresses exerted by cells on their matrix. These stresses serve as proxy for how well focal adhesions are organized and connected to the underlying contractile cytoskeleton. We found that the traction stress magnitude was always increased during infection (Figures 6A–6C; Video S5) compared to uninfected cells, which remained at steady state with minimal fluctuations (Figures S6A–S6D). Although the average traction stress magnitude appeared lower in ERK-inhibited versus control samples, this difference was not statistically significant. We also measured transepithelial electrical resistance (TEER) to

examine changes in monolayer barrier integrity and permeability (Figure S6E). Infected samples exhibited reduced TEER compared to non-infected samples, regardless of pharmacological treatment, indicating that infection compromises monolayer barrier integrity independently of ERK waves. However, since TEER provides only a scalar value representing the overall permeability of the entire monolayer without offering spatial information, this conclusion should be interpreted with caution.

Since we have established that infected and surrounder cells exhibit different mechanical properties, we quantified average traction stresses for each cell population separately and found that infected cells exerted 30% less traction compared to surrounders, while ERK inhibition attenuated this difference by 10% (Figure 6D). Monolayer stress microscopy[35] revealed that proximal surrounders failed to increase their monolayer stresses when ERK was inhibited, consistent with the model predictions that stress reinforcement is crucial for infected cell squeezing (Figures 6A and 6E). Accordingly, control infected cells displayed an approximately 30% decrease in monolayer stresses as compared to surrounder cells, while in ERK-inhibited samples, both surrounders and infected cells exhibited lower monolayer stresses than control samples (Figures 6A, 6E, and S6C and S6D). This is consistent with the model prediction, suggesting that an increase in monolayer stresses of proximal surrounders is required for infected cell squeezing (case 2). However, we do not have direct evidence that infected cell contractility is decreased (case 4), which would explain the enlargement of infected cells when ERK waves are absent.

Consistent with our previous findings,[8] the *in silico* model also predicts that differences in stiffness between infected versus surrounder cells promote squeezing, though the effect is subtle (case 2 versus 3). To further investigate this, we examined whether stiffness differences between infected versus surrounder cells at 24 hpi persist when ERK is inhibited at 4 hpi. We found that both infected and surrounder cells exhibited stiffness levels similar to uninfected samples (Figure 6F). Similar results were obtained when ERK is constitutively activated with PMA to abrogate waves (Figure S6F). Collectively, we discovered that in the absence of ERK waves, infected and surrounder cells display similar stiffness and attenuated differences in traction stress exertion. Under these conditions, proximal surrounders are unable to reinforce their monolayer stresses, a prerequisite for infected cell squeezing and CICE to occur.

ERK activation waves drive CICE in *S.f.*-infected epithelial cells *in vitro* and *in vivo*

Intracellular bacterial pathogens such as *S.f.*, which, like *L.m.,* use actin-based motility to move within host cells, have been shown to trigger ERK activation in other host cell types.[36,37] We thus examined whether *S.f.* infection of epithelial cells would also induce ERK waves and CICE. Thus, we monitored ERK

(B and C) Median (top) and heatmap plots (bottom) of ERK activity over time for uninfected (B) and *L.m.*-infected (C) MDCK cells monolayers treated with vehicle control (left), 50 μM PD0325901 (middle), or 200 nM PMA (right). Heatmap plots show individual cells' ERK activity over time (h or hpi), and cells are ordered as a function of distance from the center of the field of view (for uninfected) or the infection focus center (infected).

(D and E) Bar plots of mean frequency of ERK waves (events/(h·mm²), (D) and ERK-activated cell cluster area (μm², (E) for uninfected and *L.m.*-infected MDCK cell monolayers. $N = 4$ independent experiments, the median of which is shown as a circle overlayed on the box plot. Lines: mean ± SD, WRST: *$p < 0.05$, ns:$p > 0.05$. See also Figure S4 and Video S3.
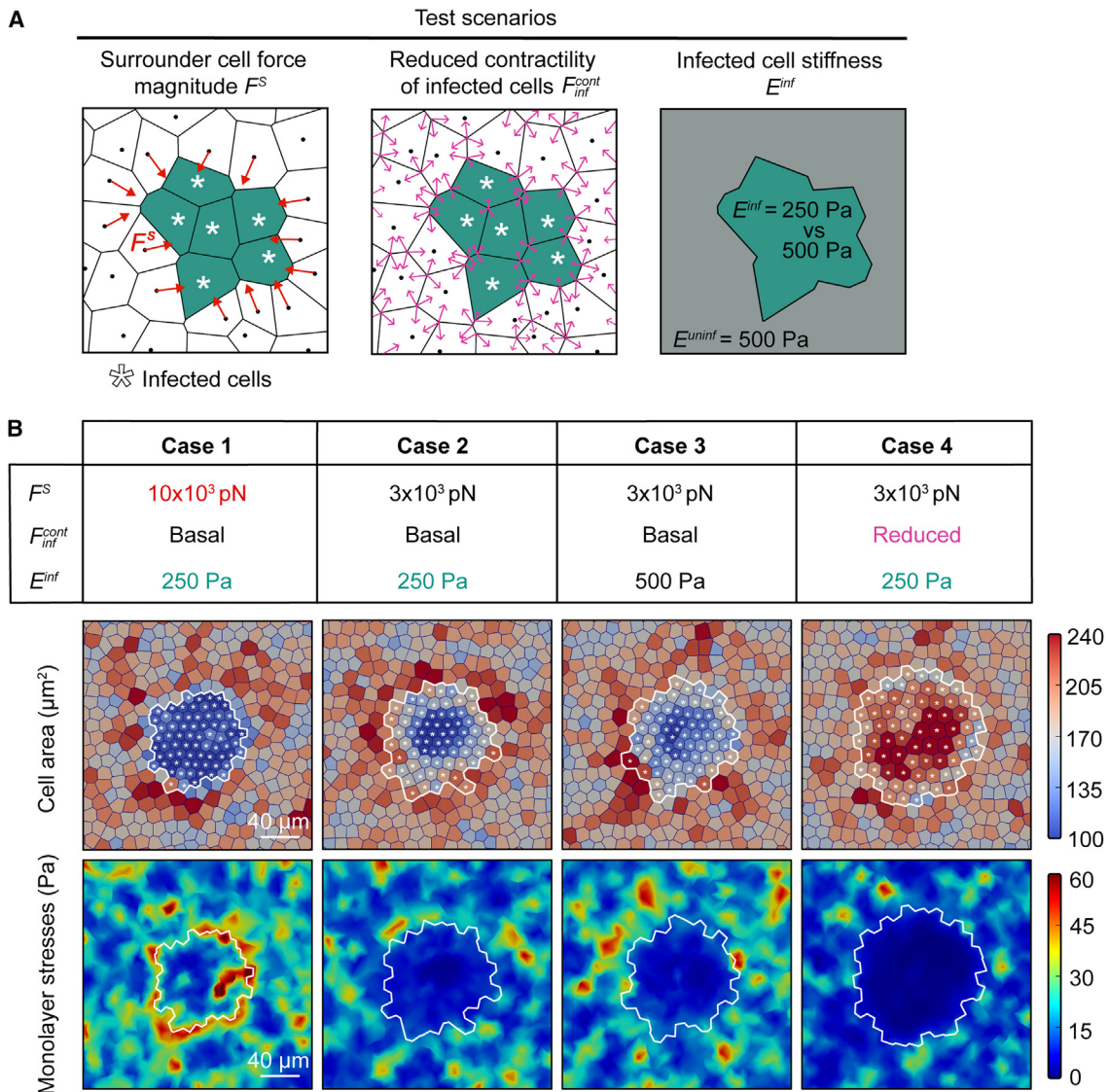
Figure 5. Modeling reveals that monolayer stress reinforcement of proximal surrounders is necessary for infected cell squeezing

(A) Schematic of hybrid model. Infected cells are denoted by green asterisk. Proximal surrounders exert force F_s pointing toward the focus (left), infected cells versus surrounders can have varying contractility (middle) or varying cell stiffness (right).

(B) Four cases were simulated (columns) by varying the parameters shown in (A). In each case, shown are the cell topology with cells color-coded by area (μm^2, top), and monolayer stresses (Pa, bottom). (1) Infected cells contract, their stiffness is half compared to surrounders, $F_s = 10 \times 10^3$ pN. (2) Infected cells contract, their stiffness is half compared to surrounders, $F_s = 3 \times 10^3$ pN. (3) Infected cells contract, their stiffness is the same as for surrounders, $F_s = 3 \times 10^3$ pN. (4) Infected cells contract less, their stiffness is half compared to surrounders, $F_s = 3 \times 10^3$ pN. White line: infection focus contour. Asterisks: infected cells. See also Figure S5 and Video S4.

activity using our FRET-based biosensor in *S.f.*-infected and uninfected MDCK cell monolayers. We observed increased ERK activity and waves during *S.f.* infection compared to uninfected cells (Figures 7A and 7B) and formation of large infection mounds and CICE in control but not ERK-inhibited *S.f.*-infected MDCK cells at 16 hpi (Figures 7C and 7D). These results showcase that changes in cell mechanics associated with ERK waves and leading to CICE likely play a crucial role in intracellular bacterial infections that trigger ERK activation and involve intercellular bacterial spread (such as *S.f.* infection).

To complement our *in vitro* and *in silico* experiments, we infected the two-layered skin epithelium of zebrafish larvae tails with *S.f.*, with or without MEK inhibitor treatment (Figure 7E). CICE occurred at 6 hpi in control infected samples but was significantly reduced in ERK-inhibited samples (Figure 7F). Additionally, in the controls, the surrounding cells were more polarized, radially aligned, and had higher shape factor than ERK-inhibited cells, consistent with the shape of surrounding MDCK cells in similar *in vitro* experiments (Figures 7E and S7A–S7F). This suggests that CICE driven by ERK-based mechanochemical competition
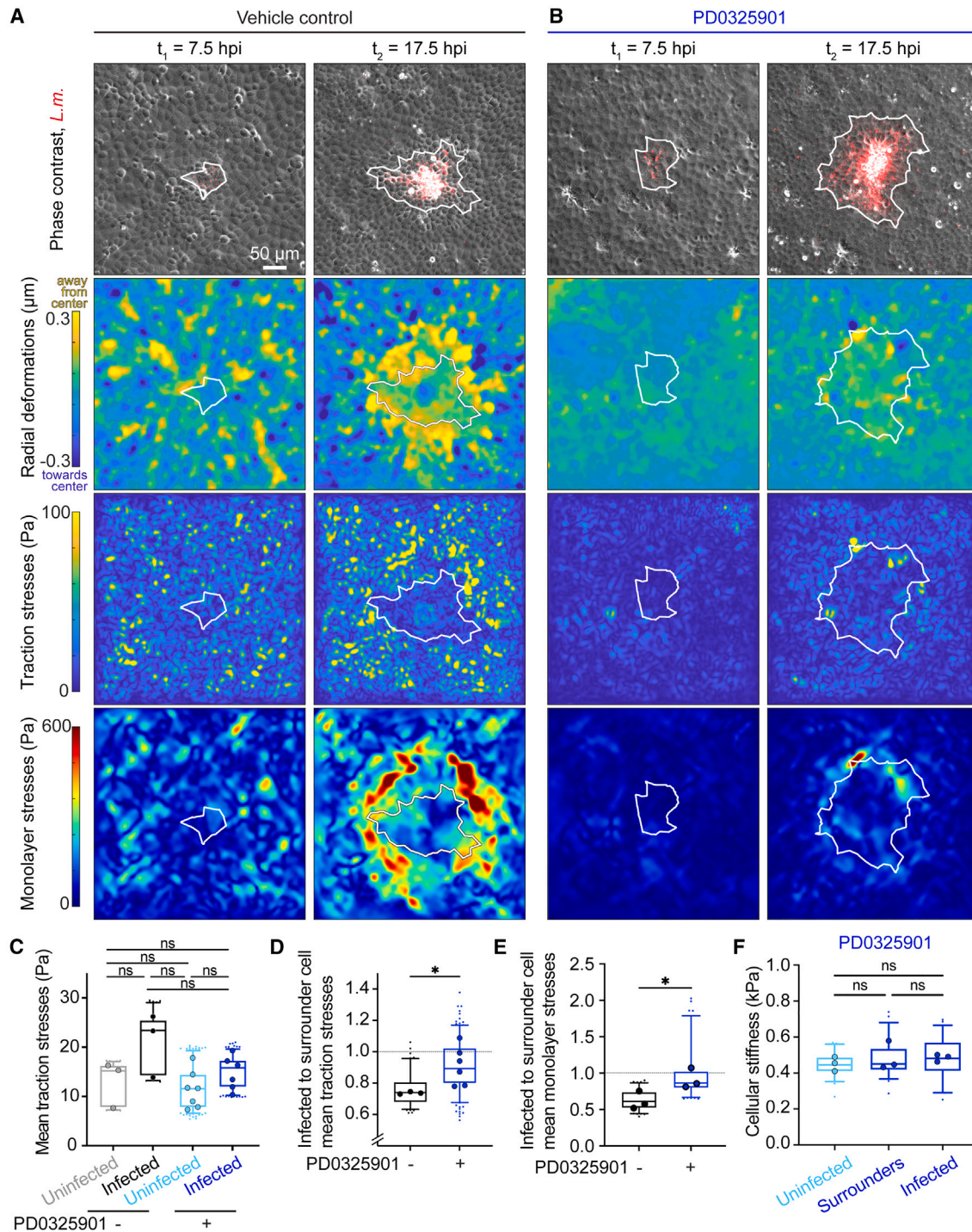
Figure 6. ERK inhibition stalls the increase in monolayer stresses in proximal surrounders and abolishes differences in stiffness between surrounders and infected cells

(A and B) TFM and MSM on MDCK cells adherent on 3-kPa gels and infected at low MOI with *L.m.* such that single-infection foci emerge. Cells were treated with vehicle control (A) or 50 μM PD0325901 (B) at 4 hpi. Rows: overlay of phase contrast with *L.m.* fluorescence, radial deformations that cells impart on their matrix (μm), traction stresses (Pa), and monolayer stresses (Pa). Columns: time (hpi). White line: infection focus contour.

(legend continued on next page)

is relevant *in vivo* and potentially in other cell types in monolayer and tissues.

DISCUSSION

Efficient clearance of bacterially infected cells from epithelial cell monolayers is critical, especially at the delicate intestine surface, where a single monolayer of cells separates the intestinal lumen from the external milieu. CICE can facilitate remodeling of the monolayer to limit infection dissemination. Here we show that ERK activation exhibits spatiotemporal variations during infection and travels in the form of waves of increased frequency between neighboring cells. The presence of these waves tilts the outcome of the mechanical battle in favor of the host and regulates CICE. In the absence of ERK waves, CICE does not occur, and the morphological and kinematical signatures of host cells associated with CICE are completely absent. Moreover, characterization of cell mechanics *in vitro* and *in silico* revealed that reinforcement of monolayer stresses of surrounder cells proximal to the infection focus is key in eliciting infected cell squeezing and CICE and does not occur in absence of ERK waves.

The implications of this work go far beyond *L.m.* infection as we demonstrated that CICE also occurs during *S.f.* infection of epithelial cells and zebrafish larvae. This provides evidence of *in vivo* CICE and opens the gates for similar investigations using other *in vivo* models. Furthermore, the proposed mechanism could be relevant in infections with pathogens other than bacteria. Supporting this idea, in monolayers of HeLa cells infected with vaccinia virus—where still images suggest the occurrence of CICE and ERK activation—it is highly likely that a similar mechanical process modulated by ERK activation waves takes place to enhance infection spread.[38] In infections with *L.m.*, we showed that ERK activation limits infection spread along the monolayer via CICE, potentially due to geometry since extruded cells cannot spread bacteria through the monolayer. Additionally, we speculate that since extruded cells eventually die due to detachment from the basement membrane, *in vivo* in the intestine they would just be discarded from the host via the fecal route.[8] This is further supported by studies on other bacterial pathogens where ERK activation occurs. For example, a study examining still images of immunostained cells showed that ERK activation in infected cells can propagate to neighboring cells, making them produce higher amounts of cytokines like IL-8, which amplifies innate immunity against infection with *L.m.*, *S.f.*, and *Salmonella typhimurium*.[36] However, infected cell squeezing or CICE was not examined or reported in this study. Interestingly, a recent clinical study involving COVID-19 also supports a model whereby ERK activation acts in favor of the host to limit infection spread.[39]

ERK wave propagation allows for fast and long-range intercellular communication in various biological contexts, including wound healing and tissue morphogenesis.[12] Here, we discovered that ERK wave propagation is also important during infection processes, such as when intracellular bacterial disseminate through epithelia, and shed light into its spatiotemporal modulation. ERK waves traveling between cells have been termed "mechanochemical" because they are closely coordinated with cell mechanics. For instance, during wound healing, ERK activation waves are synchronized with cell strain and cooperate with cell polarization to drive collective cell migration.[15] Additionally, ERK is mechanosensitive, meaning that cell extension, including mechanical stretch applied to cells, leads to ERK activation and subsequent cell contraction. We observed a similar pattern when analyzing displacements of cells during ERK wave propagation, and also that abrogation of waves results in lack of polarization of surrounder uninfected cells, necessary for CICE.

Intercellular adhesions are essential for propagation of ERK waves from cell to cell. For instance, in αE-catenin knockout (KO) cells, which are unable to form robust intercellular junctions in monolayer, ERK oscillates within individual cells but fails to propagate between them in waves.[15] We previously found that in αE-catenin KO cells, CICE is inhibited.[8] This finding, along with additional evidence presented herein where ERK is either inhibited or constitutively activated, supports the idea that ERK activity waves—rather than baseline ERK activity alone—regulate CICE. Interestingly, a study on mammary epithelial cells found that ERK activity is heightened when cells reside on stiffer matrices compared to softer ones, although the study did not assess ERK wave propagation.[40] We also previously observed that MDCK cells residing on stiffer matrices exhibit enhanced CICE as compared to those on softer matrices due to stronger traction and monolayer stresses in uninfected cells surrounding the infection focus.[41] Herein we consistently show that in the absence of ERK waves, the monolayer stress reinforcement in surrounding cells is absent, and CICE does not occur.

In vitro and *in vivo* studies have shown that during apoptosis, ERK activation propagates from the apoptotic cell(s) and then spreads to neighboring cells in waves as a mechanism to ensure the removal of damaged cells while maintaining homeostasis during tissue remodeling or in response to damage.[16,42] During infection, when CICE occurs, we did not observe clear radial waves traveling away from the infection mound toward the surrounders.[8] Accordingly, the infected cells that get extruded are not apoptotic and blocking apoptosis using different pharmacological agents does not decrease the volume of infection mounds.[41] Instead, cell death appears to be a consequence of extrusion rather than the cause of it. The question that remains unanswered is what triggers ERK activation ERK to begin with and its propagation subsequently. We speculate that the trigger could be secreted pro-inflammatory ligands for EGFR and other receptors, as recently shown.[19,23] Indeed, we previously showed that various cytokines that can activate ERK, including IL-8 and

(C) Box plots of mean traction stresses of *L.m.*-infected or not MDCK cells, treated or not with 50 μM PD0325901. ANOVA, ns: $p > 0.05$. (D and E) Box plots of ratio of traction stresses (D) or monolayer stresses (E) of infected to surrounder cells. WRST: $*p < 0.05$. For (C-E) $N = 3$ independent experiments were analyzed for cells followed from 10 to 16 hpi, dots show the mean of each sample.

(F) Box plots of cell stiffness (kPa) at 24 hpi for uninfected, surrounder cells, and infected cells, for samples treated with 50 μM PD0325901 at 4 hpi. $N = 58\pm3$ cells were analyzed in each case originating from three independent experiments. ANOVA: ns: $p > 0.05$. See also Figure S6 and Video S5.
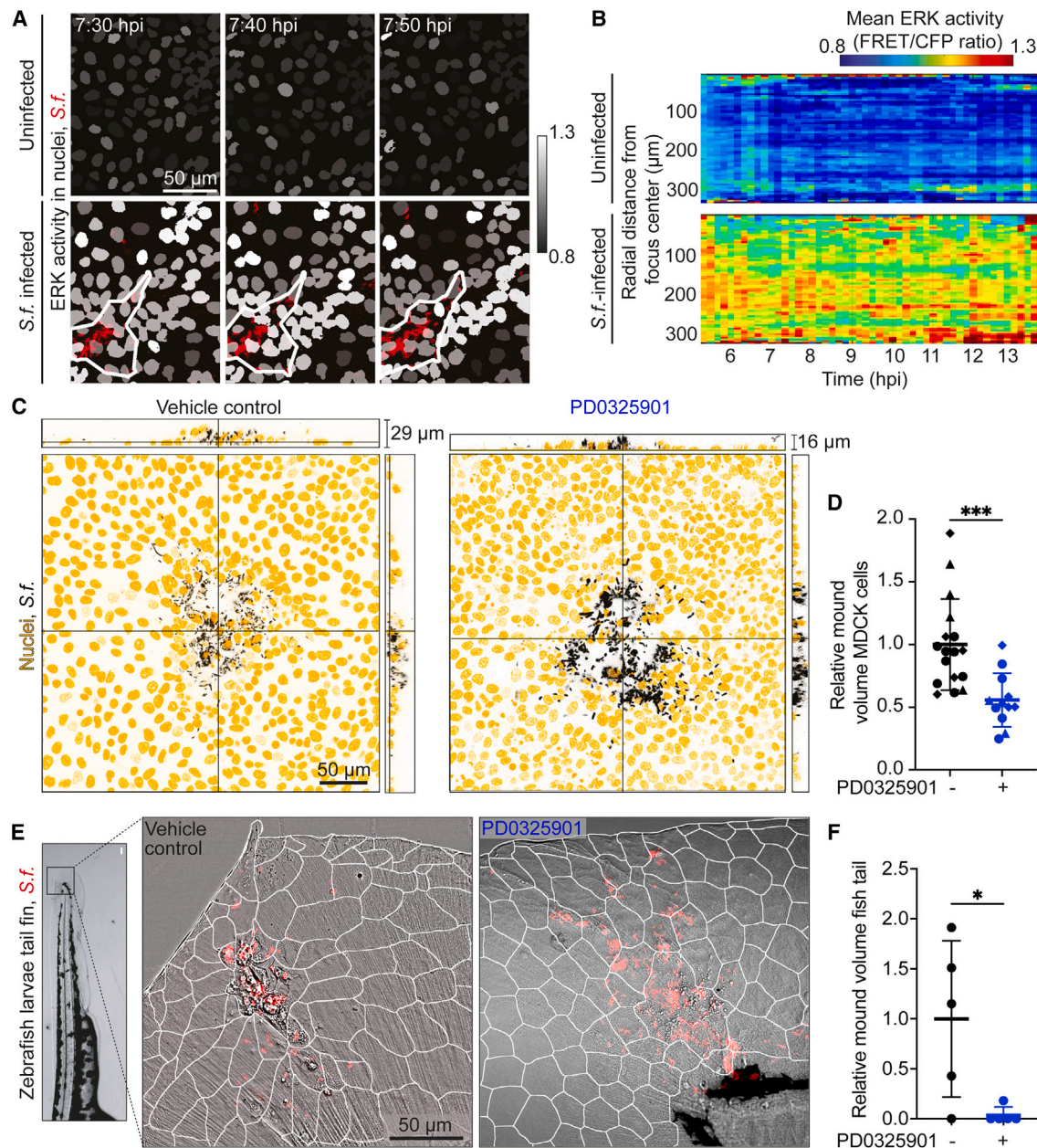
Figure 7. ERK waves also drive collective extrusion of *S.f.*-infected cells *in vitro* and *in vivo*

(A) Representative snapshots of ERK activity in the nuclei of uninfected (top) and *S.f.*-infected MDCK cells (bottom) overlayed with *S.f.* fluorescence (red). Columns: three consecutive time points (hpi).

(B) Kymograph of mean radial ERK activity (y axis) versus time (hpi, x axis) for uninfected (top) or *S.f.*-infected MDCK cells (bottom) (see Figure S4F).

(C) Orthogonal views of *S.f.*-infected MDCK cells 16 hpi treated with vehicle control (left) or 50 μM PD0325901 (right) at 4 hpi. Host nuclei: yellow; *S.f.*: black.

(D) Relative mound volume of *S.f.*-infected MDCK cells treated with vehicle control or 50 μM PD0325901. Normalization to mean of control cells. Mean ± SD, WRST: ***$p < 0.001$.

(E) Representative overlay of phase-contrast images with *S.f.* fluorescence (red) of zebrafish larvae fin tails treated with vehicle control or 41 μM PD0325901. White lines: cell contours. Image on left shows the location of the area imaged in zebrafish larvae.

(F) Relative mound volume of *S.f.*-infected extruded epithelial cells from the skin of zebrafish larvae fin tails. Samples inspected at 6 hpi. Normalization with respect to mean of control zebrafish fin tails. Mean ± SD, WRST: *$p < 0.05$. See also Figure S7.

MCP-1,[8] are present in large amounts in infected samples, and these same cytokines can increase ERK wave frequency also in non-infected cell monolayers.[23,43] However, various additional molecular mechanisms could lead to ERK activation,[12] namely (1) decrease in intercellular space volume, increasing ligand concentration and triggering EGFR-MEK/ERK signaling[44]; (2) opening of stretch-activated ion channels, leading to calcium influx and ERK activation[14]; (3) disruption of E-cadherin/EGFR heterotrimeric complex due to elevated intercellular tension, enabling EGFR dimerization and downstream signaling upon ligand binding[45]; (4) decreased membrane tension, leading to increased endocytic ERK signaling[46]; and (5) increased integrin clustering at focal adhesions.[47] The increase in traction stresses in infected cell samples from the onset of our recordings (early infection) corroborates integrin-mediated ERK activation (5). Opening of stretch-activated ion channels (2) or disruption of E-cadherin/EGFR complex due to increased monolayer stresses (3) could play a role later in infection, when uninfected surrounders become polarized and increase their cell stiffness and monolayer tension. Further experiments are required to confirm these hypotheses.

Our discovery that ERK waves orchestrate the mechanical cell competition occurring during infection and leading to CICE highlights that the interplay between cell-generated physical forces and biochemical signaling critically dictates infection outcomes.

Limitations of the study

We used the EKAREV biosensor to spatiotemporally track ERK activity during epithelial cell infection via FRET. A limitation of this biosensor is its potential responsiveness to cyclin-dependent kinase 1 (CDK1) in addition to ERK, which can lead to increased FRET/CFP signals during mitosis, even when MEK inhibitors are present.[18] Therefore, the observed decrease in ERK activity over time may partly reflect CDK1 activity during cell division. While we demonstrated the occurrence of CICE in zebrafish larvae skin epithelia, we did not explore this process in other relevant tissues, such as the intestine or lung (common entry points for pathogens), nor did we explore the role of host immune cells like macrophages and neutrophils. This could be explored in the future by using zebrafish deficient in immune cells,[48] and considering other sites of infection, including the zebrafish gut. Additionally, we did not account for the influence of extracellular physical cues in our assays, such as cell stretching[41] and ECM stiffness,[41] which could impact CICE dynamics by modulating ERK waves. Incorporating organotypic devices that simulate these conditions will be useful for understanding how biomechanical factors regulate CICE.

RESOURCE AVAILABILITY

Lead contact

Further information and requests for reagents may be directed to and will be fulfilled by the lead contact Effie Bastounis (effie.bastounis@uni-tuebingen.de) (E.E.B.).

Materials availability

Materials developed in this study are available on request to the corresponding authors.

Data and code availability

Data collected are available on request to the corresponding authors. The (phospho)proteomics data (raw files) generated during this study and subsequent analysis are available on the PRIDE repository[49] of proteomeXchange (https://proteomecentral.proteomexchange.org/ui) with identifier PRIDE: PXD055809. Analyzed (phospho)proteomic data and differential expression analysis are in Table S1. All codes are uploaded in our GitHub repository with the corresponding accession numbers as listed as follows: (1) ERK waves analysis using ARCOS (https://doi.org/10.5281/zenodo.14287824); (2) Calculation of volume of extruded infected cells calculation (https://doi.org/10.5281/zenodo.14287679); (3) Calculation of infection focus area (https://doi.org/10.5281/zenodo.14287812); (4) Cell kinematics analysis (https://doi.org/10.5281/zenodo.7155531) (5) Monolayer stresses calculation (https://doi.org/10.5281/zenodo.7155523); and (6) Hybrid computational model (https://doi.org/10.5281/zenodo.14289212).

AUTHOR CONTRIBUTIONS

Conceptualization, E.E.B. and L.H.; methodology, E.E.B., M.J.G.-B., S.M., B.M., T.E.S., L.H., M.M., R.A.-Y.; software, E.E.B; L.H., M.M., R.A.-Y., J.C.S.R., A.V.; investigation, E.E.B., L.H., M.M., R.A.-Y., A.B., A.V., Y.-T.Y., K.W., D.B., G.Ö.G.; writing – original draft, E.E.B., L.H., M.J.G.-B.; writing – review & editing, E.E.B., L.H., I.C., M.J.G.-B., R.A-Y.; resources, E.E.B., M.J.G.-B., S.M., B.M., T.E.S.; supervision, E.E.B., M.J.G.-B., S.M., B.M., T.E.S.

DECLARATION OF INTERESTS

The authors declare no competing interests.

STAR★METHODS

Detailed methods are provided in the online version of this paper and include the following:

- KEY RESOURCES TABLE
- EXPERIMENTAL MODEL AND STUDY PARTICIPANT DETAILS
  - Mammalian cell culture
  - Establishment of MDCK cells expressing the FRET-based ERK activity biosensor
  - Bacterial strains used in this study

- ○ Zebrafish larvae used in this study
- ● METHOD DETAILS
  - ○ Bacterial infections of MDCK cells in monolayer
  - ○ Injection of zebrafish larvae tail fin with *S.f*
  - ○ Reagents for pharmacological perturbations
  - ○ Fixation of MDCK cells and quantitative microscopy for calculation of infection mound volume, infection focus area, and total bacterial fluorescence intensity
  - ○ Fixation and quantitative microscopy for characterization of cell shape
  - ○ Time-lapse (FRET) microscopy imaging
  - ○ Characterization of cell kinematics and migration coordination
  - ○ Characterization of ERK activity dynamics in (infected) MDCK cells in monolayer
  - ○ Polyacrylamide hydrogel fabrication and 2D traction force microscopy
  - ○ Calculation of cell monolayer stresses
  - ○ Transepithelial electrical resistance (TEER) measurements of MDCK cells in monolayer
  - ○ Western blotting analysis
  - ○ Determination of bulk cell stiffness using atomic force microscopy (AFM)
  - ○ Sample preparation for phosphoproteomics, nano LC-MS/MS analysis and data processing
  - ○ Hybrid computational model to simulate infection *in silico*
- ● QUANTIFICATION AND STATISTICAL ANALYSIS

SUPPLEMENTAL INFORMATION

Supplemental information can be found online at https://doi.org/10.1016/j.celrep.2024.115193.

REFERENCES

1. Gouin, E., Welch, M.D., and Cossart, P. (2005). Actin-based motility of intracellular pathogens. Curr. Opin. Microbiol. *8*, 35–45. https://doi.org/10.1016/j.mib.2004.12.013.

2. Stevens, J.M., Galyov, E.E., and Stevens, M.P. (2006). Actin-dependent movement of bacterial pathogens. Nat. Rev. Microbiol. *4*, 91–101. https://doi.org/10.1038/nrmicro1320.

3. Duncan-Lowey, J.K., Wiscovitch, A.L., Wood, T.E., Goldberg, M.B., and Russo, B.C. (2020). Shigella flexneri disruption of cellular tension promotes intercellular spread. Cell Rep. *33*, 108409. https://doi.org/10.1016/j.celrep.2020.108409.

4. Lamason, R.L., Bastounis, E., Kafai, N.M., Serrano, R., Del Álamo, J.C., Theriot, J.A., and Welch, M.D. (2016). Rickettsia Sca4 reduces vinculin-mediated intercellular tension to promote spread. Cell *167*, 670–683.e10. https://doi.org/10.1016/j.cell.2016.09.023.

5. Ortega, F.E., Koslover, E.F., and Theriot, J.A. (2019). Listeria monocytogenes cell-to-cell spread in epithelia is heterogeneous and dominated by rare pioneer bacteria. Elife *8*, e40032. https://doi.org/10.7554/eLife.40032.

6. Bastounis, E.E., Radhakrishnan, P., Prinz, C.K., and Theriot, J.A. (2022). Mechanical forces govern interactions of host cells with intracellular bacterial oathogens. Microbiol. Mol. Biol. Rev. *86*, e0009420. https://doi.org/10.1128/mmbr.00094-20.

7. Rajabian, T., Gavicherla, B., Heisig, M., Müller-Altrock, S., Goebel, W., Gray-Owen, S.D., and Ireton, K. (2009). The bacterial virulence factor InlC perturbs apical cell junctions and promotes cell-to-cell spread of Listeria. Nat. Cell Biol. *11*, 1212–1218. https://doi.org/10.1038/ncb1964.

8. Bastounis, E.E., Serrano-Alcalde, F., Radhakrishnan, P., Engström, P., Gómez-Benito, M.J., Oswald, M.S., Yeh, Y.-T., Smith, J.G., Welch, M.D., García-Aznar, J.M., and Theriot, J.A. (2021). Mechanical competition triggered by innate immune signaling drives the collective extrusion of bacterially infected epithelial cells. Dev. Cell *56*, 443–460.e11. https://doi.org/10.1016/j.devcel.2021.01.012.

9. Engstrom, P., Burke, T.P., Mitchell, G., Ingabire, N., Mark, K.G., Golovkine, G., Iavarone, A.T., Rape, M., Cox, J.S., and Welch, M.D. (2019). Evasion of autophagy mediated by Rickettsia surface protein OmpB is critical for virulence. Nat. Microbiol. *4*, 2538–2551. https://doi.org/10.1038/s41564-019-0583-6.

10. Yang, J., Antin, P., Berx, G., Blanpain, C., Brabletz, T., Bronner, M., Campbell, K., Cano, A., Casanova, J., Christofori, G., et al. (2020). Guidelines and definitions for research on epithelial–mesenchymal transition. Nat. Rev. Mol. Cell Biol. *21*, 341–352. https://doi.org/10.1038/s41580-020-0237-9.

11. Olea-Flores, M., Zuñiga-Eulogio, M.D., Mendoza-Catalán, M.A., Rodríguez-Ruiz, H.A., Castañeda-Saucedo, E., Ortuño-Pineda, C., Padilla-Benavides, T., and Navarro-Tito, N. (2019). Extracellular-signal regulated kinase: A central molecule driving epithelial-mesenchymal transition in cancer. Int. J. Mol. Sci. *20*, 2885. https://doi.org/10.3390/ijms20122885.

12. Crozet, F., and Levayer, R. (2023). Emerging roles and mechanisms of ERK pathway mechanosensing. Cell. Mol. Life Sci. *80*, 355. https://doi.org/10.1007/s00018-023-05007-z.

13. Sano, T., Kobayashi, T., Negoro, H., Sengiku, A., Hiratsuka, T., Kamioka, Y., Liou, L.S., Ogawa, O., and Matsuda, M. (2016). Intravital imaging of mouse urothelium reveals activation of extracellular signal-regulated kinase by stretch-induced intravesical release of ATP. Phys. Rep. *4*, e13033. https://doi.org/10.14814/phy2.13033.

14. Gudipaty, S.A., Lindblom, J., Loftus, P.D., Redd, M.J., Edes, K., Davey, C.F., Krishnegowda, V., and Rosenblatt, J. (2017). Mechanical stretch triggers rapid epithelial cell division through Piezo1. Nature *543*, 118–121. https://doi.org/10.1038/nature21407.

15. Hino, N., Rossetti, L., Marín-Llauradó, A., Aoki, K., Trepat, X., Matsuda, M., and Hirashima, T. (2020). ERK-Mediated mechanochemical waves direct collective cell polarization. Dev. Cell *53*, 646–660.e8. https://doi.org/10.1016/j.devcel.2020.05.011.

16. Aoki, K., Kumagai, Y., Sakurai, A., Komatsu, N., Fujita, Y., Shionyu, C., and Matsuda, M. (2013). Stochastic ERK activation induced by noise and cell-to-cell propagation regulates cell density-dependent proliferation. Mol. Cell *52*, 529–540. https://doi.org/10.1016/j.molcel.2013.09.015.

17. Aoki, K., Kondo, Y., Naoki, H., Hiratsuka, T., Itoh, R.E., and Matsuda, M. (2017). Propagating wave of ERK activation orients collective cell migration. Dev. Cell *43*, 305–317.e5. https://doi.org/10.1016/j.devcel.2017.10.016.

18. Ishii, M., Tateya, T., Matsuda, M., and Hirashima, T. (2021). Retrograde ERK activation waves drive base-to-apex multicellular flow in murine cochlear duct morphogenesis. Elife *10*, e61092. https://doi.org/10.7554/eLife.61092.

19. Gagliardi, P.A., Grädel, B., Jacques, M.-A., Hinderling, L., Ender, P., Cohen, A.R., Kastberger, G., Pertz, O., and Dobrzyński, M. (2023). Automatic detection of spatio-temporal signaling patterns in cell collectives. J. Cell Biol. *222*, e202207048. https://doi.org/10.1083/jcb.202207048.

20. Boocock, D., Hino, N., Ruzickova, N., Hirashima, T., and Hannezo, E. (2021). Theory of mechanochemical patterning and optimal migration in cell monolayers. Nat. Phys. *17*, 267–274. https://doi.org/10.1038/s41567-020-01037-7.

21. Ram, A., Murphy, D., DeCuzzi, N., Patankar, M., Hu, J., Pargett, M., and Albeck, J.G. (2023). A guide to ERK dynamics, part 1: mechanisms and models. Biochem. J. *480*, 1887–1907. https://doi.org/10.1042/bcj20230276.

22. Davies, A.E., Pargett, M., Siebert, S., Gillies, T.E., Choi, Y., Tobin, S.J., Ram, A.R., Murthy, V., Juliano, C., Quon, G., et al. (2020). Systems-level properties of EGFR-RAS-ERK signaling amplify local signals to generate

dynamic gene expression heterogeneity. Cell Syst. *11*, 161–175.e5. https://doi.org/10.1016/j.cels.2020.07.004.

23. DeCuzzi, N.L., Oberbauer, D., Chmiel, K.J., Pargett, M., Ferguson, J.M., Murphy, D., Hardy, M., Ram, A., Zeki, A.A., and Albeck, J.G. (2024). Spatiotemporal clusters of ERK activity coordinate cytokine-induced Inflammatory responses in human airway epithelial cells. Am. J. Resp. Cell Mol. https://doi.org/10.1165/rcmb.2024-0256OC.

24. Wang, W., Zhang, Y., Dettinger, P., Reimann, A., Kull, T., Loeffler, D., Manz, M.G., Lengerke, C., and Schroeder, T. (2021). Cytokine combinations for human blood stem cell expansion induce cell-type- and cytokine-specific signaling dynamics. Blood *138*, 847–857. https://doi.org/10.1182/blood.2020008386.

25. Kinoshita, N., Hashimoto, Y., Yasue, N., Suzuki, M., Cristea, I.M., and Ueno, N. (2020). Mechanical stress regulates epithelial tissue integrity and stiffness through the FGFR/Erk2 signaling pathway during embryogenesis. Cell Rep. *30*, 3875–3888.E3. https://doi.org/10.1016/j.celrep.2020.02.074.

26. Moreno, E., Valon, L., Levillayer, F., and Levayer, R. (2019). Competition for Space Induces Cell Elimination through Compaction-Driven ERK Downregulation. Curr. Biol. *29*, 23–34.E8. https://doi.org/10.1016/j.cub.2018.11.007.

27. Aikin, T.J., Peterson, A.F., Pokrass, M.J., Clark, H.R., and Regot, S. (2020). MAPK activity dynamics regulate non-cell autonomous effects of oncogene expression. Elife *9*, e60541. https://doi.org/10.7554/eLife.60541.

28. Gagliardi, P.A., Dobrzyński, M., Jacques, M.-A., Dessauges, C., Ender, P., Blum, Y., Hughes, R.M., Cohen, A.R., and Pertz, O. (2021). Collective ERK/Akt activity waves orchestrate epithelial homeostasis by driving apoptosis-induced survival. Dev. Cell *56*, 1712–1726.E6. https://doi.org/10.1016/j.devcel.2021.05.007.

29. Young, M.D., Wakefield, M.J., Smyth, G.K., and Oshlack, A. (2010). Gene ontology analysis for RNA-seq: accounting for selection bias. Genome Biol. *11*, R14. https://doi.org/10.1186/gb-2010-11-2-r14.

30. Mitchel, J.A., Das, A., O'Sullivan, M.J., Stancil, I.T., DeCamp, S.J., Koehler, S., Ocaña, O.H., Butler, J.P., Fredberg, J.J., Nieto, M.A., et al. (2020). In primary airway epithelial cells, the unjamming transition is distinct from the epithelial-to-mesenchymal transition. Nat. Commun. *11*, 5053. https://doi.org/10.1038/s41467-020-18841-7.

31. Zeldovich, V.B., Robbins, J.R., Kapidzic, M., Lauer, P., and Bakardjiev, A.I. (2011). Invasive extravillous trophoblasts restrict intracellular growth and spread of Listeria monocytogenes. PLoS Pathog. *7*, e1002005. https://doi.org/10.1371/journal.ppat.1002005.

32. Ortega, F.E., Rengarajan, M., Chavez, N., Radhakrishnan, P., Gloerich, M., Bianchini, J., Siemers, K., Luckett, W.S., Lauer, P., Nelson, W.J., and Theriot, J.A. (2017). Adhesion to the host cell surface is sufficient to mediate Listeria monocytogenes entry into epithelial cells. Mol. Biol. Cell *28*, 2945–2957. https://doi.org/10.1091/mbc.E16-12-0851.

33. Pond, K.W., Morris, J.M., Alkhimenok, O., Varghese, R.P., Cabel, C.R., Ellis, N.A., Chakrabarti, J., Zavros, Y., Merchant, J.L., Thorne, C.A., and Paek, A.L. (2022). Live-cell imaging in human colonic monolayers reveals ERK waves limit the stem cell compartment to maintain epithelial homeostasis. Elife *11*, e78837. https://doi.org/10.7554/eLife.78837.

34. Komatsu, N., Aoki, K., Yamada, M., Yukinaga, H., Fujita, Y., Kamioka, Y., and Matsuda, M. (2011). Development of an optimized backbone of FRET biosensors for kinases and GTPases. Mol. Biol. Cell *22*, 4647–4656. https://doi.org/10.1091/mbc.e11-01-0072.

35. Bazellières, E., Conte, V., Elosegui-Artola, A., Serra-Picamal, X., Bintanel-Morcillo, M., Roca-Cusachs, P., Muñoz, J.J., Sales-Pardo, M., Guimerà, R., and Trepat, X. (2015). Control of cell–cell forces and collective cell dynamics by the intercellular adhesome. Nat. Cell Biol. *17*, 409–420. https://doi.org/10.1038/ncb3135.

36. Kasper, C.A., Sorg, I., Schmutz, C., Tschon, T., Wischnewski, H., Kim, M.L., and Arrieumerlou, C. (2010). Cell-cell propagation of NF-kappaB transcription factor and MAP kinase activation amplifies innate immunity

against bacterial infection. Immunity *33*, 804–816. https://doi.org/10.1016/j.immuni.2010.10.015.

37. Köhler, H., Rodrigues, S.P., and McCormick, B.A. (2002). Shigella flexneri Interactions with the Basolateral Membrane Domain of Polarized Model Intestinal Epithelium: Role of Lipopolysaccharide in Cell Invasion and in Activation of the Mitogen-Activated Protein Kinase ERK. Infect. Immun. *70*, 1150–1158. https://doi.org/10.1128/iai.70.3.1150-1158.2002.

38. Beerli, C., Yakimovich, A., Kilcher, S., Reynoso, G.V., Fläschner, G., Müller, D.J., Hickman, H.D., and Mercer, J. (2019). Vaccinia virus hijacks EGFR signalling to enhance virus spread through rapid and directed infected cell motility. Nat. Microbiol. *4*, 216–225. https://doi.org/10.1038/s41564-018-0288-2.

39. Witowski, A., Palmowski, L., Rahmel, T., Nowak, H., Ehrentraut, S.F., Putensen, C., von Groote, T., Zarbock, A., Babel, N., Anft, M., et al. (2024). Activation of the MAPK network provides a survival advantage during the course of COVID-19-induced sepsis: a real-world evidence analysis of a multicenter COVID-19 Sepsis Cohort. Infection. https://doi.org/10.1007/s15010-024-02325-7.

40. Farahani, P.E., Lemke, S.B., Dine, E., Uribe, G., Toettcher, J.E., and Nelson, C.M. (2021). Substratum stiffness regulates Erk signaling dynamics through receptor-level control. Cell Rep. *37*, 110181. https://doi.org/10.1016/j.celrep.2021.110181.

41. Aparicio-Yuste, R., Muenkel, M., Clark, A.G., Gómez-Benito, M.J., and Bastounis, E.E. (2022). A Stiff Extracellular Matrix Favors the Mechanical Cell Competition that Leads to Extrusion of Bacterially-Infected Epithelial Cells. Front. Cell Dev. Biol. *10*, 912318. https://doi.org/10.3389/fcell.2022.912318.

42. Hiratsuka, T., Fujita, Y., Naoki, H., Aoki, K., Kamioka, Y., and Matsuda, M. (2015). Intercellular propagation of extracellular signal-regulated kinase activation revealed by in vivo imaging of mouse skin. Elife *4*, e05178. https://doi.org/10.7554/eLife.05178.

43. Werle, M., Schmal, U., Hanna, K., and Kreuzer, J. (2002). MCP-1 induces activation of MAP-kinases ERK, JNK and p38 MAPK in human endothelial cells. Cardiovasc. Res. *56*, 284–292. https://doi.org/10.1016/S0008-6363(02)00600-4.

44. Tschumperlin, D.J., Dai, G., Maly, I.V., Kikuchi, T., Laiho, L.H., McVittie, A.K., Haley, K.J., Lilly, C.M., So, P.T.C., Lauffenburger, D.A., et al. (2004). Mechanotransduction through growth-factor shedding into the extracellular space. Nature *429*, 83–86. https://doi.org/10.1038/nature02543.

45. Sullivan, B., Light, T., Vu, V., Kapustka, A., Hristova, K., and Leckband, D. (2022). Mechanical disruption of E-cadherin complexes with epidermal growth factor receptor actuates growth factor-dependent signaling. Proc. Natl. Acad. Sci. USA *119*, e2100679119. https://doi.org/10.1073/pnas.2100679119.

46. De Belly, H., Stubb, A., Yanagida, A., Labouesse, C., Jones, P.H., Paluch, E.K., and Chalut, K.J. (2021). membrane tension gates ERK-mediated regulation of pluripotent cell fate. Cell Stem Cell *28*, 273–284.e6. https://doi.org/10.1016/j.stem.2020.10.018.

47. Guo, W.h., and Wang, Y.l. (2007). Retrograde fluxes of focal adhesion proteins in response to cell migration and mechanical signals. Mol. Biol. Cell *18*, 4519–4527. https://doi.org/10.1091/mbc.e07-06-0582.

48. Shiau, C.E., Kaufman, Z., Meireles, A.M., and Talbot, W.S. (2015). Differential requirement for irf8 in formation of embryonic and adult macrophages in zebrafish. PLoS One *10*, e0117513. https://doi.org/10.1371/journal.pone.0117513.

49. Perez-Riverol, Y., Bai, J., Bandla, C., García-Seisdedos, D., Hewapathirana, S., Kamatchinathan, S., Kundu, D.J., Prakash, A., Frericks-Zipper, A., Eisenacher, M., et al. (2022). The PRIDE database resources in 2022: a hub for mass spectrometry-based proteomics evidences. Nucleic Acids Res. *50*, D543–D552. https://doi.org/10.1093/nar/gkab1038.

50. Bernardini, M.L., Mounier, J., d'Hauteville, H., Coquis-Rondon, M., and Sansonetti, P.J. (1989). Identification of icsA, a plasmid locus of Shigella flexneri that governs bacterial intra- and intercellular spread through

interaction with F-actin. Proc. Natl. Acad. Sci. USA *86*, 3867–3871. https://doi.org/10.1073/pnas.86.10.3867.

51. Perez, T.D., Tamada, M., Sheetz, M.P., and Nelson, W.J. (2008). Immediate-early signaling induced by E-cadherin engagement and adhesion. J. Biol. Chem. *283*, 5014–5022. https://doi.org/10.1074/jbc.M705209200.

52. Ellett, F., Pase, L., Hayman, J.W., Andrianopoulos, A., and Lieschke, G.J. (2011). mpeg1 promoter transgenes direct macrophage-lineage expression in zebrafish. Blood *117*, e49–e56. https://doi.org/10.1182/blood-2010-10-314120.

53. Kawabata, N., and Matsuda, M. (2016). cell density-dependent increase in tyrosine-monophosphorylated ERK2 in MDCK cells expressing active Ras or Raf. PLoS One *11*, e0167940. https://doi.org/10.1371/journal.pone.0167940.

54. Schindelin, J., Arganda-Carreras, I., Frise, E., Kaynig, V., Longair, M., Pietzsch, T., Preibisch, S., Rueden, C., Saalfeld, S., Schmid, B., et al. (2012). Fiji: an open-source platform for biological-image analysis. Nat. Methods *9*, 676–682.

55. Cox, J., and Mann, M. (2008). MaxQuant enables high peptide identification rates, individualized p.p.b.-range mass accuracies and proteome-wide protein quantification. Nat. Biotechnol. *26*, 1367–1372. https://doi.org/10.1038/nbt.1511.

56. Tyanova, S., Temu, T., Sinitcyn, P., Carlson, A., Hein, M.Y., Geiger, T., Mann, M., and Cox, J. (2016). The Perseus computational platform for comprehensive analysis of (prote)omics data. Nat. Methods *13*, 731–740. https://doi.org/10.1038/nmeth.3901.

57. Franceschini, A., Szklarczyk, D., Frankild, S., Kuhn, M., Simonovic, M., Roth, A., Lin, J., Minguez, P., Bork, P., Von Mering, C., and Jensen, L.J. (2013). STRING v9. 1: protein-protein interaction networks, with increased coverage and integration. Nucleic Acids Res. *41*, D808–D815. https://doi.org/10.1093/nar/gks1094.

58. Wilkinson, L. (2011). ggplot2: Elegant Graphics for Data Analysis (Springer).

59. Mostowy, S., Boucontet, L., Mazon Moya, M.J., Sirianni, A., Boudinot, P., Hollinshead, M., Cossart, P., Herbomel, P., Levraud, J.P., and Colucci-Guyon, E. (2013). The zebrafish as a new model for the in vivo study of Shigella flexneri interaction with phagocytes and bacterial autophagy. PLoS Pathog. *9*, e1003588. https://doi.org/10.1371/journal.ppat.1003588.

60. Bastounis, E.E., Radhakrishnan, P., Prinz, C.K., and Theriot, J.A. (2021). Volume measurement and biophysical characterization of mounds in epithelial monolayers after intracellular bacterial infection. STAR Protoc. *2*, 100551. https://doi.org/10.1016/j.xpro.2021.100551.

61. Pentecost, M., Kumaran, J., Ghosh, P., and Amieva, M.R. (2010). Listeria monocytogenes Internalin B activates junctional endocytosis to accelerate intestinal invasion. PLoS Pathog. *6*, e1000900. https://doi.org/10.1371/journal.ppat.1000900.

62. Wang, X., Merkel, M., Sutter, L.B., Erdemci-Tandogan, G., Manning, M.L., and Kasza, K.E. (2020). Anisotropy links cell shapes to tissue flow during convergent extension. Proc. Natl. Acad. Sci. USA *117*, 13541–13551. https://doi.org/10.1073/pnas.1916418117.

63. Gui, L., and Wereley, S.T. (2002). A correlation-based continuous window-shift technique to reduce the peak-locking effect in digital PIV image evaluation. Exp. Fluids *32*, 506–517. https://doi.org/10.1007/s00348-001-0396-1.

64. Angelini, T.E., Hannezo, E., Trepat, X., Fredberg, J.J., and Weitz, D.A. (2010). Cell migration driven by cooperative substrate deformation patterns. Phys. Rev. Lett. *104*, 168104. https://doi.org/10.1103/PhysRevLett.104.168104.

65. del Álamo, J.C., Meili, R., Alonso-Latorre, B., Rodríguez-Rodríguez, J., Aliseda, A., Firtel, R.A., and Lasheras, J.C. (2007). Spatio-temporal analysis of eukaryotic cell motility by improved force cytometry. Proc. Nat. Acad. Sci. USA *104*, 13343–13348. https://doi.org/10.1073/pnas.0705815104.

66. Bastounis, E.E., Ortega, F.E., Serrano, R., and Theriot, J.A. (2018). a multi-well format polyacrylamide-based assay for studying the effect of extracellular matrix stiffness on the bacterial infection of adherent cells. J. Vis. Exp. *137*, 57361. https://doi.org/10.3791/57361.

67. Muenkel, M., Aparicio-Yuste, R., Tal, M.C., Kraiczy, P., and Bastounis, E.E. (2022). Spatiotemporal characterization of endothelial cell motility and physical forces during exposure to Borrelia burgdorferi. STAR Protoc. *3*, 101832. https://doi.org/10.1016/j.xpro.2022.101832.

68. Yuste, R.A., Muenkel, M., Axarlis, K., Gómez Benito, M.J., Reuss, A., Blacker, G., Tal, M.C., Kraiczy, P., and Bastounis, E.E. (2022). Borrelia burgdorferi modulates the physical forces and immunity signaling in endothelial cells. iScience *25*, 104793. https://doi.org/10.1016/j.isci.2022.104793.

69. Bastounis, E., Meili, R., Álvarez-González, B., Francois, J., del Álamo, J.C., Firtel, R.A., and Lasheras, J.C. (2014). Both contractile axial and lateral traction force dynamics drive amoeboid cell motility. J. Cell Biol. *204*, 1045–1061. https://doi.org/10.1083/jcb.201307106.

70. Tambe, D.T., Hardin, C.C., Angelini, T.E., Rajendran, K., Park, C.Y., Serra-Picamal, X., Zhou, E.H., Zaman, M.H., Butler, J.P., Weitz, D.A., et al. (2011). Collective cell guidance by cooperative intercellular forces. Nat. Mater. *10*, 469–475. https://doi.org/10.1038/nmat3025.

71. Zittlau, K.I., Lechado-Terradas, A., Nalpas, N., Geisler, S., Kahle, P.J., and Macek, B. (2022). temporal analysis of protein ubiquitylation and phosphorylation during parkin-dependent mitophagy. Mol. Cell. Proteomics *21*, 100191. https://doi.org/10.1016/j.mcpro.2021.100191.

72. Boersema, P.J., Raijmakers, R., Lemeer, S., Mohammed, S., and Heck, A.J.R. (2009). Multiplex peptide stable isotope dimethyl labeling for quantitative proteomics. Nat. Protoc. *4*, 484–494. https://doi.org/10.1038/nprot.2009.21.

73. Gonzalez-Valverde, I., and Garcia-Aznar, J.M. (2017). A hybrid computational model to explore the topological characteristics of epithelial tissues. Int. J. Numer. Method Biomed. Eng *33*, e2877. https://doi.org/10.1002/cnm.2877.

74. Sarkar, D., Gompper, G., and Elgeti, J. (2021). A minimal model for structure, dynamics, and tension of monolayered cell colonies. Commun. Phys. *4*, 36. https://doi.org/10.1038/s42005-020-00515-x.

STAR★METHODS

KEY RESOURCES TABLE

REAGENT or RESOURCE	SOURCE	IDENTIFIER
Antibodies		
Anti-EGFR rabbit antibody	Cell Signaling	Cat#4267;RRID:AB_2797654
Anti-pEGFR rabbit antibody	Cell Signaling	Cat#3777;RRID:AB_2096270
Anti-pERK1/2 rabbit antibody	Cell Signaling	Cat#9101;RRID:AB_331646
Anti-ERK mouse antibody	BD Biosciences	Cat#610124;RRID:AB_397530
Anti-pMEK1/2 rabbit antibody	Cell Signaling	Cat#9121;RRID:AB_331648
Anti-MEK1/2 rabbit antibody	Cell Signaling	Cat#9122;RRID:AB_823567
Human anti-GAPDH antibody	Bio-Rad	Cat#12004168;RRID:AB_2941791
IRDye 680RD Goat anti-mouse	Li-Cor	Cat#92568070;RRID:AB_2651128
IRDye 800CW Goat anti-rabbit	Li-Cor	Cat#92632211;RRID:AB_621843
Bacterial and virus strains		
L. monocytogenes: *L.m.*-ActAp:mTagRFP	Ortega et al.[32]	N/A
L. monocytogenes: *L.m.*-GFP	Ortega et al.[32]	N/A
S. flexneri M90T	Bernardini et al.[50]	N/A
Chemicals, peptides, and recombinant proteins		
DMEM	Thermo Fisher	Cat#41965039
FluoroBrite DMEM	Thermo Fisher	Cat#A1896701
Phosphate buffered saline (PBS)	Thermo Fisher	Cat#10010023
Fetal bovine serum (FBS)	Thermo Fisher	Cat#10270106
L-glutamine	PanReac-AppliChem	Cat#A3704
Blasticidin S	Sigma	Cat#SBR00022
MS-222 (tricaine)	Sigma-Aldrich	Cat#A5040
PTU	Sigma-Aldrich	Cat#P7629
BBL Brain Heart Infusion (BHI)	BD	Cat#211059
Difco Agar, granulated	BD	Cat#214530
Streptomycin sulfate	Thermo Fisher	Cat#455340050
Chloramphenicol	Corning	Cat#56-75-7
Gentamicin	Fisher	Cat#15820243
Tryptone soya agar (TSA)	Sigma-Aldrich	Cat#22091
Carbenicillin	Sigma-Aldrich	Cat#C1389
Congo red solution	Sigma-Aldrich	Cat# C6767
Tryptone soya broth (TSB)	Sigma-Aldrich	Cat#T8907
Phenol red	Sigma-Aldrich	Cat#P0290
Polyvinyl-pyrrolidone (PVP)	Sigma-Aldrich	Cat#PVP40
NaCl	Sigma	Cat#S7653
KCl	Sigma	Cat#P9541
CaCl dihydrate	Sigma	Cat#21102
MgSO4 hexahydrate	Sigma	Cat#M2670
MEK inhibitor PD0325901	Sigma	Cat#PZ0162
Dimethyl sulfoxide (DMSO)	Sigma	Cat#D2650
Low-melting point agarose	Thermo Fisher	Cat#R0801
Sulfo-SANPAH	Fisher	Cat#10474005
Collagen I, rat tail	Thermo Fisher	Cat#A1048301
Phorbol 12-myristate 13-acetate (PMA)	Sigma	Cat#P1585

(Continued on next page)

Continued

REAGENT or RESOURCE	SOURCE	IDENTIFIER
MEK inhibitor trametinib	Selleckchem	Cat#S2673
Human EGF	Sigma	Cat#E9644
EGFR inhibitor PD153035	Sigma	Cat#SML0564
Hoechst 33342	Invitrogen	Cat#H3570
Formaldehyde 16% methanol-free	Thermo Fisher	Cat#28906
Bovine serum albumin (BSA)	AppliChem	Cat#A6588
(3-Aminopropyl)triethoxysilane	Sigma	Cat#A3648
40% Acrylamide	Sigma	Cat#A4058-100ML
Bis-acrylamide solution (2%w/v)	Fisher Scientific	Cat#BP1404-250
FluoSpheres carboxylate-modified microspheres, 0.2 μm, yellow-green fluorescent (505/515)	Invitrogen	Cat#F8803
Ammonium persulfate	Fisher	Cat#BP17925
TEMED	Sigma	Cat#T9281-25ML
HEPES, free acid	J.T. Baker	Cat#4018-04
0.25% trypsin-EDTA, phenol red	Thermo Fisher	Cat#25200056
Benzonase	Merck	Cat#70746
SCH772984	Selleckchem	Cat# S7156
Marimastat	Selleckchem	Cat# S7156
Deposited data		
Phosphoproteomic data	This paper	ProteomeXchange, PRIDE: PXD055809
Experimental models: Cell lines		
MDCK II	Perez et al.[51]	N/A
MDCK II E-cadherin-GFP	Perez et al.[51]	N/A
Experimental models: Organisms/strains		
WT AB strain zebrafish	Ellett et al.[52]	N/A
Recombinant DNA		
pT2A-EKAREV-NLS plasmid	Kawabata et al.[53]	N/A
Software and algorithms		
Fiji	Schindelin et al.[54]	RRID:SCR_002285 https://imagej.net/
MATLAB	The MathWorks Inc.	RRID:SCR_001622 https://de.mathworks.com/products/matlab.html
GraphPad Prism	GraphPad	RRID:SCR_002798 http://www.graphpad.com/scientific-software/prism/
NIS-Elements software package	Nikon	RRID:SCR_014329 https://www.nikoninstruments.com/Products/Software
Igor Pro	WaveMetrics, Lake Oswego, OR, USA	RRID:SCR_000325 http://www.wavemetrics.com/products/igorpro/igorpro.htm
MaxQuant software suite (version 1.6.14.0)	Cox et al.[55]	RRID:SCR_014485 https://www.maxquant.org/
Perseus software (version 1.6.3.2)	Tyanova et al.[56]	RRID:SCR_015753 https://maxquant.net/perseus/
STRING software	Franceschini et al.[57]	RRID:SCR_005223 http://string.embl.de/

(Continued on next page)

Continued

REAGENT or RESOURCE	SOURCE	IDENTIFIER
R package ggplot2	Wilkinson et al.[58]	RRID:SCR_014601 https://cran.r-project.org/web/packages/ggplot2/index.html
ERK waves analysis using ARCOS	This paper	https://doi.org/10.5281/zenodo.14287824
Calculation of volume of extruded infected cells	This paper	https://doi.org/10.5281/zenodo.14287679
Calculation of infection focus area	This paper	https://doi.org/10.5281/zenodo.14287812
Cell kinematics analysis	This paper	https://doi.org/10.5281/zenodo.7155531
Monolayer stresses calculation	Aparicio-Yuste et al.[68]	https://doi.org/10.5281/zenodo.7155523
Hybrid computational model	This paper	https://doi.org/10.5281/zenodo.14289212

EXPERIMENTAL MODEL AND STUDY PARTICIPANT DETAILS

Mammalian cell culture

Epithelial type II Madin-Darby Canine Kidney (MDCK) cells (originally provided by Nelson lab, Stanford University) were cultured in high glucose DMEM medium (Thermo Fisher, 41965039) containing 4.5 g/L glucose and supplemented with 10% fetal bovine serum (FBS, Thermo Fisher, 10270106) in a 5% CO_2 humidified incubator at 37°C. The cell passages were between P10-P50. During image acquisition, the cells were cultured under the same conditions as indicated above, except that FluoroBrite DMEM (Thermo Fisher, A1896701) supplemented with 580 mg/L L-glutamine (PanReac-AppliChem, A3704) and 10% FBS was used as cell culture medium. To image the localization of E-cadherin over time with live-cell time-lapse microscopy, we used type II MDCK E-cadherin GFP expressing cells (MDCK E-cadherin-GFP, kindly provided by the Nelson lab, Stanford University).[51] For FRET-based time-lapse imaging of ERK activity in the nuclei of MDCK cells, we used cells transfected with the pT2A-EKAREV-NLS (kindly provided by Hirashima lab, Mechanobiology Institute, Singapore).[15,34,53]

Establishment of MDCK cells expressing the FRET-based ERK activity biosensor

For the establishment of EKAREV-NLS-expressing MDCK cells, type II MDCK cells were transfected with the plasmid pT2A-EKAREV-NLS using the Neon transfection system (Invitrogen, MPK5000). Briefly, type II MDCK cells were resuspended in the resuspension buffer at a concentration of 1×10^6 cells in 100 μL and gently pipetted to get a single-cell suspension. Twenty-four-well glass bottom plates were filled with 0.5 mL of complete cell culture medium and preincubated in the incubator at 37°C with 5% CO_2. Ten microliters of the plasmid at a concentration of 1.5 μg/mL was added in the cell suspension and cells were electroporated in 10-μL tips using the following electroporation parameters: pulse voltage: 1650 V; pulse width: 20 ms; pulse number: 1. Following electroporation, the 10 μL of cell and plasmid suspension was added in one well of the 24-well plate. Medium was replenished the following day and two days later when cells had proliferated, 10 μg/mL blasticidin (Sigma, SBR00022) was added for selection. Once cells formed a monolayer, fluorescence microscopy was used to confirm that approximately 90% of cells were expressing the plasmid. To obtain a pure population of MDCK cells expressing the pT2A-EKAREV-NLS plasmid the transfected cells were flow-sorted with the MA900 cell sorter. Thereon, the cells were propagated in medium always supplemented with 10 μg/mL of blasticidin.

Bacterial strains used in this study

The *Listeria monocytogenes* (*L.m.*) strains used in this study are as follows: JAT607 (Species: *L.m.* 1043S, Genotype/Description: ActApmTagRFP),[32] and JAT605 (Species: *L.m.* 1043S, Genotype/Description: Constitutive GFP).[32] The *Shigella flexneri* (*S.f.*) strain used in this study is *S.f.* srv. 5a str. M90T constitutively expressing mCherry.[59]

Zebrafish larvae used in this study

Animal experiments were performed according to the Animals (Scientific Procedures) Act 1986 and approved by the Home Office (Project license: PPL P4E664E3C). Zebrafish embryos were obtained by natural spawning, and larvae were maintained at 28.5°C in E3 embryo medium unless otherwise stated. E3 medium contained 5 mM NaCl (Sigma, S7653), 0.17 mM KCl (Sigma, P9541), 0.33 mM CaCl dihydrate (Sigma, 21102), and 0.33 mM MgSO4 hexahydrate (Sigma, M2670) in distilled water. The AB wildtype zebrafish strain was used. For injections and live imaging, embryos were anesthetized in 200 μg/mL MS-222 (tricaine) (Sigma-Aldrich, A5040) in E3 and recovered into fresh E3 supplemented with 0.036 g/L PTU (Sigma-Aldrich, P7629).

METHOD DETAILS

Bacterial infections of MDCK cells in monolayer

Listeria monocytogenes (*L.m.*) infection of MDCK cells in monolayer was performed as described previously[60] using the *L.m.* 10403S strain JAT607 ActApmTagRFP. This strain expresses mTagRFP under the control of the ActA promoter, which is activated once the

bacteria have invaded the host cell, leading to intracellular fluorescent bacteria approximately 4 hpi.[5] In few assays where an alternative fluorescent protein was needed (e.g., when staining cells with propidium iodine to assess cell death), infection was done using the 10403S *L.m.* strain constitutively expressing GFP.[61] Briefly, the bacteria were streaked out from a frozen glycerol stock onto BHI (BD, 211059) agar (BD, 214530) plates with 0.2 mg/mL streptomycin (Thermo Fisher Scientific, 455340050) and 7.5 μg/mL chloramphenicol (Corning, 56-75-7) and then maintained at 37°C for 2 days. To get flagellated *L.m.* prior to infection, cultures of 2 mL of 37 g/L BHI, 0.2 mg/mL streptomycin and 7.5 μg/mL chloramphenicol were inoculated from colonies on the BHI agar plates, and kept in the dark at room temperature without shaking for ~16 h, that is, until the cultures had reached an optical density (OD$_{600}$) of approximately 0.5. Afterward, the cultures were centrifuged at 2000 x *g* at room temperature for 5 min and resuspended in 2.5 mL DMEM cell culture medium. The bacterial L.*m.*-suspension was diluted 1:16 in medium to get a multiplicity of infection (MOI) of 100–200 bacteria/host cell, as determined by plating different dilutions of the *L.m.*-suspension on BHI agar plates and counting the colonies formed after 1–2 days. The volume of *L.m.*-suspension added on the cell monolayers depended on the assay: we used 0.25 mL per 24-well transwell insert, 1 mL per 24-well plate well, 1.5 mL per AFM cell culture dish, 2 mL per 6-well plate well, and 12 mL per T-175 flask. The confluent host cell monolayers were incubated with the *L.m.*-suspension in a 5% CO$_2$ humidified incubator at 37°C for 30 min. Afterward, host cells were washed four times with phosphate buffered saline (PBS, Thermo Fisher, 10010023) and finally DMEM was added containing 20 μg/mL gentamicin (Fisher, 15820243).

The *Shigella flexneri* (*S.f.*) infection was performed like *L.m.*-infections with pathogen specific modifications. The *S.f.* strain srv. 5a str. M90T constitutively expressing mCherry was streaked out from a frozen glycerol stock on 40 g/L tryptone soya agar (TSA, Sigma-Aldrich, 22091) with 100 μg/mL carbenicillin (Sigma-Aldrich, C1389) and 1% Congo red solution (Sigma-Aldrich, C6767) which identifies colonies containing the virulence plasmid. For the overnight culture, 5 mL of tryptone soya broth (TSB, Sigma-Aldrich, T8907) containing 100 μg/mL carbenicillin were inoculated with a virulent red colony. The bacterial *S.f.*-suspension for infection was prepared 2–2.5 h before infection by inoculating 100 μL of *S.f.* overnight culture in 5 mL TSB containing 100 μg/mL of carbenicillin, followed by incubation at 37°C and 200 rpm until the cultures reached an OD$_{600}$ of about 0.6 (1.5–2 h). As with infection of MDCK with *L.m.*, 100% confluent MDCK cell monolayers were infected with 1 mL *S.f.*-infection mix, which corresponded to a MOI of 5 bacteria/host cell. This was followed by centrifugation at 200 x *g* for 10 min, incubation for 30 min, washing away extracellular bacteria four times and finally adding medium containing 50 μg/mL of gentamicin, to ensure killing of extracellular bacteria in the cell culture medium that might result from lysis of infected cells. The MDCK monolayers were only infected for 16 h before being fixed, since we found that *S.f.* spread intercellularly faster than *L.m.* and first extruded infected cells were observed at approx. 6 hpi as opposed to approx. 15 h when infected with *L.m.*

Injection of zebrafish larvae tail fin with *S.f*

S.f. cultures for injection were prepared as mentioned earlier, with minor adjustments. Following overnight growth, 5 mL of TSB containing 100 μg/mL of carbenicillin was inoculated with 100 μL of the overnight culture and incubated at 37°C, shaking at 200 rpm until the OD$_{600}$ reached approximately 0.3-0.5. Bacteria were then pelleted by centrifugation at 4000 x *g* for 4 min at room temperature. Bacteria were washed in PBS resuspended in a mixture of phenol red (Sigma-Aldrich, P0290) and polyvinyl-pyrrolidone (PVP, Sigma-Aldrich, PVP40) (final concentration 0.25% phenol red and 2% PVP) to a concentration of 10,000 CFU/nL. Embryos were injected into the tail fin with 1–2 nL of inoculum and recovered into petri dishes containing either E3 + 41 μM PD0325901 (Sigma, PZ0162) or E3 + DMSO (Sigma, D2650) as a vehicle control. At 6 hpi, *S.f.* infected embryos were immobilized in 1% low-melting point agarose (Thermo Fisher, R0801) and positioned on glass-bottom MatTek dishes. Imaging was performed with a Zeiss LSM 880 with Fast Airyscan and 63x/1.4 NA oil objective. For fixed samples, *S.f.* infected embryos were collected at 6 hpi and fixed in 4% methanol-free paraformaldehyde (PFA, Thermo Fisher, 28906) at 4°C overnight. Embryos were washed in PBS and imaged as above.

Reagents for pharmacological perturbations

Pharmacological perturbations were applied on MDCK cells at 4 hpi or later when indicated, by replacing the cell culture medium with medium containing either vehicle control or the indicated pharmacological inhibitor or molecule. For MEK inhibition, we cultured cells in 50 μM PD0325901. Stock concentration was 41 mM in DMSO, and we used as vehicle control the same volume of DMSO. ERK was activated in cell culture with 200 nM Phorbol 12-Myristate 13-Acetate (PMA, Sigma, P1585) and stock concentration was 1.62 mM in DMSO. Trametinib (MEK inhibitor, Selleckchem, S2673) concentration used in cell culture was 200 nM and the stock concentration was 10 mM. EGF (Sigma, E9644-.2MG) was used in cell culture at a concentration of 10 and 25 ng/mL and the stock concentration was 10 μg/mL. PD153035 (EGFR inhibitor, Sigma, SML0564-5MG) was used in cell culture at a concentration of 4 μM and stock concentration was 5 mM in DMSO.

Fixation of MDCK cells and quantitative microscopy for calculation of infection mound volume, infection focus area, and total bacterial fluorescence intensity

For analysis of infection foci, MDCK cell nuclei were stained by replacing the medium with 5 μg/mL Hoechst (Invitrogen, H3570) containing cell culture medium at 4 hpi (more details in section "Bacterial infections of MDCK cells in monolayer"). Samples were incubated at 37°C and 5% CO$_2$ for 10 min. Subsequently, samples were washed once with pre-warmed PBS and cell culture medium containing 20 μg/mL of gentamicin was added. The samples were fixed 24 hpi or 16 hpi for *L.m.*- or *S.f.*- infected MDCK samples,

respectively, by carefully washing once with warm PBS, then adding 500 µL of 4% PFA diluted in PBS per well for 10 min, followed by washing with and storing the samples in PBS at 4°C until imaging.

For 3D imaging of infection mounds different spinning disk confocal microscopes were used, depending on where and when the experiments where performed. Infection mounds (resulting from *L.m.* infection) were initially imaged with a Zeiss AxioObserver SD Spinning Disk microscope, with an Axiocam 503 mono CCD camera and a Plan-Apochromat 40x/1.4 NA Oil DIC objective (University of Stuttgart). Samples infected with *L.m.* and treated with TPA, EGF, PMA, trametinib, and the EGFR inhibitor were imaged with our newly installed spinning disk confocal microscope, a Nikon Eclipse Ti2 microscope equipped with a CSU-W1 spinning disc with 50-µm Disk and a digital camera C15440 (Hamamatsu), using a 40x/1.25 NA silicon oil objective. Finally, infection mounds resulting from *S.f.* infection of MDCKs were imaged using a Zeiss LSM 880 with Fast Airyscan and 40x/1.2 NA oil immersion objectives.

In all cases described earlier and irrespective of the microscope, z stack confocal images of the bacterial fluorescence and host MDCK nuclei fluorescence were acquired with a z-spacing between 0.2 and 1 µm. Fields of view were selected so that the whole mound could be imaged in all conditions investigated. To quantify the infection mound volume (i.e., the volume occupied by collectively extruded infected cells) from the resulting images, we used custom written MATLAB (The MathWorks Inc., RRID:SCR_001622) codes available at: https://github.com/ebastoun/Infection_mound_volume. In brief, the nuclei fluorescence images were first background corrected, then binarized and finally the MATLAB function alphaShape was applied to calculate the area covered by extruded nuclei per z-plane, disregarding the basal cell monolayer. The alpha radius used was 50 px. The volume of the extruded infected cells was determined by adding up the area of each z slice and multiplying by the increment between each z slice as described previously.[41,60] The calculated mound volumes were normalized to the mean of the control condition (without pharmacological perturbations, i.e., vehicle control) for each independent experiment.

To quantify the area of the infection foci (i.e., the domain occupied by neighboring infected cells) and the total *L.m.* fluorescence intensity of the infection foci (proxy of bacterial load within each focus), we performed epifluorescence imaging of the fixed samples. We used an inverted Nikon Eclipse Ti2 microscope with a Prime 95B camera (Teledyne Photometrics) using a 40x/0.6 NA air objective and the NIS-Elements (RRID:SCR_014329) software package. The bacterial fluorescence images were analyzed with the alphaShape function (alpha radius 50 px) to infer the area of the infection foci, as described previously[5] and using custom-written codes in MATLAB available at: https://github.com/ebastoun/Infection_mound_area_over_time. The bacterial load of each infection focus was calculated by integrating the bacterial fluorescence intensity values within the infection focus area. For each independent experiment values were normalized relative to the mean of the control condition (i.e., to the condition without pharmacological perturbations).

Fixation and quantitative microscopy for characterization of cell shape

For cell shape quantification of MDCK cells in the uninfected and *L.m.*-infected monolayers, the infection assay was performed using MDCK E-cadherin-GFP cells because E-cadherin localizes at the cell-cell junctions and thus enables accurate segmentation of the cells comprising the monolayer (more details in section "Bacterial infections of MDCK cells in monolayer"). As described in the section above, the live-cell samples were Hoechst-stained and then fixed 24 hpi. Phase-contrast and epifluorescence imaging (of nuclei, E-cadherin, and bacterial fluorescence) was performed with an inverted Nikon Eclipse Ti2 microscope with a Prime 95B camera using a 20X/0.7 NA super plan fluor LWD ADM air objective and the NIS-Elements software package. The E-cadherin fluorescence images were segmented with the Fiji plugin Tissue Analyzer.[54] The segmented image was then used as input for a custom written MATLAB code to determine for each cell in the image: (1) the cell area, (2) the radial alignment angle of the major axis of the cell, (3) the aspect ratio of the cell (ratio of the length of the major axis to minor axis), (4) the shape factor determined as the ratio of the cell perimeter to square root of cell area. The radial alignment angle is defined as the angle formed between the radial direction (center of field of view which in the infected samples coincides approximately with the center of the infection focus) and direction of the major axis of the cell. Moreover, while the aspect ratio quantifies the elongation/polarization of each cell, the shape factor parameter is an indicator of the shear rigidity (or tissue fluidity) of the cells, with a shape factor of 3.81 indicating cells behaving more like solids and higher values more fluid-like cells.[62] To discriminate between infected cells and their uninfected surrounders in the *L.m.*-infected MDCK monolayers, we used the bacterial fluorescence images and cells were classified as infected if their maximum bacterial fluorescence intensity exceeded a threshold value empirically determined.

Time-lapse (FRET) microscopy imaging

To characterize cell migration and ERK activity of uninfected and *L.m.*-infected MDCK monolayers, live-cell epifluorescence microscopy imaging and FRET imaging was performed. To that end, glass-bottom 24-well plates (Cellvis, P24-1.5H-N) were coated with 30 µg/mL rat-tail collagen I at 37°C for 30 min. Then, we seeded $2*10^5$ MDCK EKAREV-NLS expressing cells per well for 24 h to form a confluent monolayer. The confluent monolayers were then infected with 1 mL/well of the bacterial *L.m.*-suspension (more details in section "Bacterial infections of MDCK cells in monolayer"). Four hpi, we washed the uninfected and *L.m.*-infected monolayers once with PBS, added FluoroBrite DMEM with pharmacological treatment or vehicle control, and started the multi-channel imaging. Phase-contrast and epifluorescence (nuclei and bacterial fluorescence) live cell imaging was performed with an inverted Nikon Eclipse Ti2 microscope with a Prime 95B camera using a 40x/0.6 NA air objective and the NIS-Elements software package. The microscope was surrounded by a box-type incubator (OKOlab) maintained at 37°C and humidified with 5% CO_2. We took images for 20–30 h every 2.5, 5, or 10 min. For FRET imaging of the ERK activity, first the CFP signal was imaged by using CFP 436/20 excitation

and 480/40 emission filters. Then, the FRET signal was imaged with CFP 436/20 excitation and YFP 535/30 emission filters. From here on, those images are referred to as CFP and FRET image, respectively. For imaging propagation of *L.m.* expressing mtagRFP, we used an mCherry filter with 560/40 excitation and 630/75 emission. For imaging of *S.f.*-infected MDCK EKAREV-NLS expressing or control uninfected cells, a similar approach was used, with the exception that a different microscopy system, the Zeiss LSM 880 with Fast Airyscan with a 20x/0.8 NA air objective, was used.

Characterization of cell kinematics and migration coordination

The time-lapse MDCK nuclei fluorescence images were used to compute the cell migration speed of the MDCK cells in monolayer and coordination of their migration. To do so, particle image velocimetry (PIV) with a window size and overlap of 48 px and 24 px, respectively, was applied on the nuclei fluorescence images.[63] We calculated the speed of migration of cells by dividing the resulting displacements to the time interval between frames, which was always 10 min. The coordination of migration was approximated by the calculation of the correlation length of movement as done previously.[64] We first calculated the spatial correlation function $C_{dd}(R)$ that averages the scalar product of all displacement vector pairs separated by a distance R. The correlation values show an exponential decay over distance that could be fitted to the function $C_{dd}(R) = \exp(-R/R_0)$, where $2R_0$ indicates the maximum non-random correlated distance.[64] The custom-written codes to calculate the correlation length were written in MATLAB and are available at: https://github.com/ebastoun/Correlation_length_of_movement_of_epithelial_cells_in_monolayer. To calculate the directionality of movement of surrounder cells and create the rose plots (Figures 3E and 3F), we tracked the movement of the cell nuclei with the Fiji v2.14.0 plugin TrackMate v7.13.2 over the duration of the time-lapse recording. The cell migration directionality angle at each instance of time was defined as the angle between the displacement of the cell nucleus, and the radial direction. For the radial direction the center of the polar coordinate system was defined either as the center of the field of view or in the case of infection as the center of the infection focus. For the construction of the histogram plots, we binned the calculated angles ranging from 0° to 180° in groups of 7.5°, where 0°/180° corresponds to a nucleus moving toward/away from the infection focus, respectively.

Characterization of ERK activity dynamics in (infected) MDCK cells in monolayer

To obtain the ERK activity in the nuclei of MDCK cells expressing EKAREV-NLS, which is represented by the FRET efficiency, the CFP (CFP/CFP) and FRET (CFP/YFP) images were background-corrected by subtracting from them the CFP and FRET fluorescence images of an empty position also imaged overtime but not containing cells. Then, the ratio of background-corrected FRET to CFP image was calculated, followed by multiplication with a binary mask of the cell nuclei to exclude regions not containing cell nuclei. That was performed with the ImageJ/Fiji binarization method "Huang". The resulting images containing the ERK activity in the nuclei of cells over time were further analyzed with two different approaches.

First, we created kymographs of the mean radial ERK activity as a function of distance away from the center of the field of view imaged (y axis) and over time (x axis). To that end, we moved to a radial coordinate system whose origin is at the center of the field of view imaged, which for infected samples coincides approximately with the center of the infection focus (see Figure S4F).

Second, instead of averaging ERK activity to create kymographs, for all the cells one-by-one (y axis, cell count) we plotted the median of ERK activity in the cell nucleus at each given instance of time (x axis) (Figure 4B). To that end, live-cell images were pre-processed with Fiji, and subsequent image processing was performed using a custom-written MATLAB script. Briefly, accurate nuclei segmentation and subsequent individual nucleus tracking was performed with the Stardist detector and TrackMate plugin v.7.12.2, respectively, in Fiji. Correction of false connections between nuclei in the segmentation mask was done with the "watershed irregular features" option, while the convexity threshold value was set to 0.99 (Biovoxxel plugin v2.6.0). A custom MATLAB script was used to read the TrackMate output file with the coordinates of each nucleus track, process the individual tracks to quantify cell orientation and match ERK intensity to nuclei tracks. The segmentation mask and ERK signal image were matched for each nucleus position at every frame. ERK activity for a single nucleus was calculated as the median of the values contained in the region of the ERK signal image defined by the segmentation mask of that nucleus. Thus, kymographic heatmaps of single cell ERK activity display ERK activity over time, where the single cell tracks of the nuclei are vertically organized by closest distance to the center of the image (Top: center; bottom: edge of the image).

We further processed the single cell ERK activity signals (code available at: https://github.com/ebastoun/Single_cell_ERK_signal_analysis) to identify clusters of ERK activated cells as well as how ERK activity propagates to neighboring cells in the form of waves. To that end, we used MATLAB v2023b and the ARCOS v0.3.0, ggplot2 v3.5.1 and sf v1.0-16 packages in R v4.4.1, as previously proposed for automatically characterizing the spatiotemporal ERK signaling patterns in cell collectives.[19] We performed this analysis in two steps. First, we performed some ERK activity signal filtering, then, the collective ERK activation events were detected and the ERK wave characteristics were quantified, as described in detail below. To accurately detect an ERK activation event in a single cell nucleus, we used a custom MATLAB script to remove the global long-term trend in ERK fluorescence intensity and also the intrinsic noise from the single cell ERK fluorescence intensity signals. The global trend was calculated with a long moving median filter (50 time points) considering the ERK signal intensity for all the cell nuclei in a given time point, and then subtracted from the single cell ERK fluorescence intensity signal. The intrinsic noise of the global-trend-filtered single cell ERK fluorescence intensity signal was calculated with a short moving median filter (30 time points) and subtracted from itself. A threshold was applied to the resulting single cell ERK fluorescence intensity signal (value of 0.02) so that values equal or higher than the threshold were considered as single cell ERK activations. The results were saved in a.csv file and then read by a custom R script to quantify the ERK activation waves with the

ARCOS algorithm as done previously.[19] Briefly, the ARCOS algorithm finds clusters of activated cell nuclei (defined as collective events) at every time point through the DBSCAN algorithm, which depends upon a search distance parameter. Then, the ARCOS algorithm groups the clusters based on its members. We chose a search distance parameter of 25.8 μm based on the distribution of distances among the cell nuclei in the first time point. For further analysis, we filtered out collective events with less than four nuclei and considered events that persist for at least two consecutive frames. Moreover, for the analysis in Figures 4D and 4E images taken from 8 to 16 hpi were considered. Using this approach we calculated (1) mean ERK activated cell cluster area for each condition under study and (2) frequency of ERK activated cell collective events, defined as the number of events per hour and normalized to the area of the field of view examined, as done previously.[19]

Polyacrylamide hydrogel fabrication and 2D traction force microscopy

How well cell-ECM adhesions are organized and connected to the underlying cytoskeleton was assessed with TFM which allows the calculation of the traction stresses that cells exert on their extracellular matrix (ECM). To perform TFM, two-layered soft elastic polyacrylamide hydrogels were prepared, where the uppermost one contained fluorescent tracer beads and was collagen I-coated to enable subsequent cell adhesion. As cells adhere, move and contract on the hydrogel, they deform it inducing traceable movement of the beads. By measuring the beads' displacements, we then calculated the traction stresses that cells exert, as described previously.[4,65,66] Using the calculated traction stresses one can infer the monolayer stresses (intra- and inter-cellular stresses) using monolayer stress microscopy, as discussed in the section below.[67,68]

Briefly, we first manufactured polayacrylamide hydrogels to serve as the cells' ECM. To that end, wells from a 24-well glass bottom plate were pretreated by incubating at room temperature with 0.5 M NaOH for 30 min, 2% APTES in 95% EtOH for 5 min and 0.5% glutaraldehyde for 30 min to 2 h, rinsed with distilled water in between each pretreating step and finally dried at 60°C. A 3 kPa stiff polyacrylamide hydrogel was prepared by mixing 5% acrylamide (Sigma, A4058-100ML) with 0.1% bis-acrylamide (Fisher BioReagents, BP1404250) in distilled water. For the preparation of the second layer, we also added 0.03% of 0.2 μm fluorescent beads to the mixture (Thermo Fisher, F8807). To initiate polymerization 0.43% TEMED (Sigma-Aldrich, 1107320100) and 0.06% ammonium persulfate (APS) were added to the first mixture. Per well, 3.6 μL of the polyacrylamide solution mixture was added on the pretreated glass surface. Immediately after, untreated 12 mm glass coverslips were pressed on top to flatten the gels. After 20 min polymerization, the glass cover slips were removed, and polymerization of the second layer mixture containing the fluorescent beads was initiated with TEMED and APS. Per well, 2.5 μL of the second layer mixture was added on top of the first layer, followed by flattening with 12 mm glass coverslips. The coverslips were removed after 20 min polymerization, the hydrogels were covered with 50 mM HEPES pH 8.5, sterilized 1h with UV, and stored at 4°C. The hydrogels were washed once with 50 mM HEPES, then activated by addition of 200 μL/well of 0.1% w/v Sulfo-SANPAH (Thermo Scientific, 10474005) with 1% DMSO in 50 mM HEPES, and UV radiation for 10 min. This was immediately followed by washing with 50 mM HEPES and addition of 200 μL/well of 0.25 mg/mL Collagen I (Thermo Fisher, A1048301) diluted in 50 mM HEPES. The plate was incubated overnight at room temperature. Before seeding of the cells on hydrogels, the hydrogels were washed with PBS and equilibrated with cell culture medium at 37°C for 30 min. To achieve confluent cell monolayers $2.5*10^5$ MDCK cells expressing EKAREV-NLS cells per well were seeded on the hydrogels and placed in a 5% CO_2 humidified incubator at 37°C. After 24 h, when MDCK had formed confluent monolayers, some wells were infected with 1 mL/well of the bacterial *L.m.*-suspension for 30 min (more details in section "Bacterial infections of MDCK cells in monolayer").

After 4 hpi, the uninfected and *L.m.*-infected monolayers were washed once with PBS and FluoroBrite DMEM with drugs or vehicle control was added, directly before the multi-channel live-cell epifluorescence microscopy imaging was to start. For imaging in all cases, we used an inverted Nikon Eclipse Ti2 microscope with a Prime 95B camera using a 40x/0.6 NA air objective and the NIS-Elements software package. The microscope was surrounded by a box-type incubator (OKOlab) maintained at 37°C, humidified and with 5% CO_2. Every 10 min for a period of 20–24 h we took the phase-contrast image of cells, the bacterial fluorescence image and the fluorescence image of the tracer beads. At the end of the TFM recording, cells were detached using 10% SDS to obtain the reference images of the fluorescent beads in the hydrogels in their undeformed configuration.

The 2D displacements of the beads were calculated in MATLAB by comparing the fluorescence bead image to the undeformed reference image at each instance of time using a method similar to particle image velocimetry (PIV).[63] The used window size and overlap of the interrogation window were 32 px and 16 px, respectively. Using these displacements the traction stresses exerted by the cell monolayers on the hydrogels were calculated in MATLAB as described before.[4,69] To differentiate the traction stresses exerted by the infected cells versus their uninfected surrounders, a custom written MATLAB code was used (available at: https://github.com/ebastoun/Infection_mound_area_over_time) to border the infected area over time. This was done with the built-in alphaShape function using an alpha radius of 50 px. With the resulting binary mask containing the area of the infected cells, the traction stresses were allocated to surrounder or infected cells.

Calculation of cell monolayer stresses

We calculated inter- and intra-cellular stresses, herein referred to as monolayer stresses, using the technique Monolayer Stress Microscopy (MSM).[70] MSM makes use of the traction forces exerted by cells on their ECM as input and assumes that these traction forces are perfectly transmitted between the monolayer and the ECM, i.e., cell-ECM adhesions are perfect. This results in cells being subjected to a force equal to traction forces but in opposite directions (third Newton's Law). Furthermore, we only consider traction forces in the plane of the monolayer, neglecting those in the vertical direction (out of plane). It is also assumed that the thickness of the

monolayer is constant and uniform. Cell-cell adhesions are assumed to be perfect (the monolayer is considered as a continuum), the mechanical properties of the monolayer are assumed to be uniform, so that cells within the monolayer can be modeled as linear elastic isotropic materials.[70] Another assumption MSM takes is that cell deformations are small, i.e., the displacements that occur between two consecutive time frames and the changes in cell shapes and areas are small. These assumptions greatly simplify the formulation of the problem, as a two-dimensional framework is adopted, with a plane stress formulation. In this case, the equilibrium equations, compatibility, and constitutive equations yield the Beltrami differential formulation. This formulation, together with Newton's equilibrium equations, formulated at each point of the monolayer in a differential way, yield the distribution of the stresses in the monolayer. The model equations are solved using the finite element formulation in a custom-built software.[68] The monolayer was discretized with square elements of size 4.5 μm × 4.5 μm, forming a finite element mesh of 10,000 elements. The Poisson's coefficient was set to 0.49. The source code is available at: https://github.com/ebastoun/Monolayer-Stress-Microscopy.

Transepithelial electrical resistance (TEER) measurements of MDCK cells in monolayer

To assess barrier integrity of (infected) MDCK cells in monolayer overtime we performed TEER measurements, using the cellZscope system (NanoAnalytics, Münster, Germany). For this, 24-well transwell inserts (0.4 μm pore size, cellQuart, 9320402) were coated with 400 μL of 30 μg/mL collagen I solution in PBS at 37°C for 30 min. This was followed by washing with PBS and seeding of $0.5*10^5$ MDCKs per insert one day before infection. Two inserts were not seeded with cells and served as blank positions. Twenty-four hours after cell seeding, when cell monolayers had formed, some were infected with 0.25 mL/insert of the bacterial *L.m.*-suspension for 30 min (more details in section "Bacterial infections of MDCK cells in monolayer"). After washing four times with PBS, all inserts were transferred from the 24-well plate to the chambers of the cellZscope system. Four hundred μL of cell culture medium supplemented with 20 μg/mL gentamicin was added in each insert and 800 μL in the chamber outside of each insert. The part of the cellZscope system containing the cells was placed in a 5% CO_2 humidified incubator at 37°C and the TEER was measured every 30 min. For drug treatment the measurement was paused 4 hpi to add 50 μM PD0325901 and DMSO as vehicle control. The TEER was monitored for 30 to 40 h.

Western blotting analysis

To determine protein expression and phosphorylation of EGFR, MEK, and ERK, in uninfected and *L.m.*-infected MDCK monolayers, western blotting was performed. First, glass-bottom 6 well plates (Cellvis, P06-1.5H-N) were coated with 2 mL of 30 μg/mL collagen I in PBS at 37°C for 30 min, washed once with PBS, and then $10*10^5$ MDCK cells/well were seeded. After 24 h, the MDCK cell monolayers were 100% confluent and were either infected with 1.5 mL/well of bacterial *L.m.*-suspension for 30 min (more details in section "Bacterial infections of MDCK cells in monolayer") or not (control uninfected monolayers). Twenty-four hours after infection, the cell samples were lysed with a buffer containing 0.5 M Tris-HCl, pH 7.4, 1.5 M NaCl, 2.5% deoxycholic acid, 10% NP-40, 10 mM EDTA and a protease inhibitor mixture (phenylmethylsulfonyl fluoride (PMSF), leupeptin, aprotinin, and sodium orthovanadate). The total cell lysate was separated on an SDS-PAGE (4% stacking, 10% running), followed by transfer onto a nitrocellulose membrane (Immobilon P, 0.45-mm pore size). Then, the membrane was incubated with the designated antibodies as follows anti-phospho-EGF receptor (EGFR, Tyr1068, Clone D7A5) rabbit monoclonal antibody (Cell Signaling, #3777, RRID:AB_2096270); anti-EGF receptor (EGFR, Clone D38B1) rabbit monoclonal antibody (Cell Signaling, #4267, RRID:AB_2797654); anti-phospho-p44/42 MAPK (Erk1/2) (Thr202/Tyr204) rabbit monoclonal antibody (Cell Signaling, #9101, RRID:AB_331646); anti-ERK (pan Erk, Clone 16/ERK) mouse monoclonal antibody (BD Biosciences, #610124, RRID:AB_397530); anti-phospho-MEK1/2 (Ser217/221) rabbit polyclonal antibody (Cell Signaling, #9121, RRID:AB_331648); anti-MEK1/2 rabbit polyclonal antibody (Cell Signaling, #9122, RRID:AB_823567); anti-GAPDH human Fab rhodamine antibody (BioRad, #12004168, RRID:AB_2941791). Immunodetection was performed using the IRDye 680RD and 800CW-labeled secondary antibodies (Li-Cor, #925–68070, RRID:AB_2651128 and #926–32211, RRID:AB_61843) under the Bio-Rad ChemiDoc imaging system. GAPDH was used as reference protein. Quantification was performed using Fiji.

To verify that 50 μM of the MEK inhibitor PD0325901 abrogates phosphorylation of ERK, we performed western blotting of *L.m.*-infected MDCK monolayers treated or not with PD0325901, using a slightly modified protocol since these experiments were performed in a different laboratory/institution. The cells were lysed 24 hpi with RIPA buffer (Thermo Fisher Scientific, 89900) supplemented with phosphatase/protease inhibitor cocktail (1:100, Cell Signaling, 5872) on ice. The lysate was transferred to precooled tubes and centrifuged at 14000 x *g* at 4°C for 20 min. The proteins in the supernatant were separated by SDS-PAGE with 15-well Bolt Mini Gels 4–12% (Invitrogen, NW04125BOX). Semi dry blotting was used to transfer the proteins from the gel to the PVDF transfer membranes (0.45 μm, Thermo Fisher, 88518). The membrane was blocked with 5% bovine serum albumin (BSA, AppliChem, A6588) in tris-buffered saline with 1% Tween (TBST) at 4°C overnight. Incubation with primary and secondary antibodies and imaging was performed as indicated in the paragraph just above.

Determination of bulk cell stiffness using atomic force microscopy (AFM)

To measure the stiffness of *L.m.*-infected cells and their uninfected surrounder cells and to compare those to the stiffness of cells originating from uninfected wells, we conducted AFM. For sample preparation, we first added 1.5 mL/dish of 30 μg/mL collagen I in PBS to glass-bottom cell culture dishes (50 mm, WPI, FD5040-100) and incubated them at 37°C for 30 min. Dishes were then washed with PBS, cells seeded with $4.6*10^5$ MDCK cells/dish and incubated for 24 h until 100% confluent monolayers had formed.

At that point, monolayers were infected with 1.5 mL/dish bacterial suspension (more details in section "Bacterial infections of MDCK cells in monolayer") or were left untreated (uninfected controls). For ERK inhibition or activation, we added 50 μM PD0325901 or 200 nM PMA to the cell culture medium at 4 hpi. After 24 hpi the AFM measurements were performed using a commercial AFM setup (MFP3D-BIO, Asylum Research, Santa Barbara, CA, USA) mounted on an inverted optical microscope (Ti-S, Nikon, Tokyo, Japan). Cantilevers with 2 μm diameter spherical tips and a nominal spring constant of 200 pN/nm (biosphere B1000-CONT, nanotools, München, Germany) were used. Before each measurement, the spring constant was calibrated using thermal calibration. Force maps (50×50 μm^2, $30x30$ px^2) were recorded. The retract distance was set to 3 μm, the sampling rate to 2 Hz and the trigger force to 500 pN. Typical sample indentations were several hundred nanometers. Data were analyzed in Igor Pro (WaveMetrics, Lake Oswego, OR, USA, RRID:SCR_000325) using the Hertz Model. Force maps typically contained several cells. Regions of interest (ROIs) of individual cells were drawn manually and the median stiffness value for each cell was calculated.

Sample preparation for phosphoproteomics, nano LC-MS/MS analysis and data processing

Samples were prepared using the protocol for "in-solution protein digestion" as previously described for two biological replicates.[71] Briefly, to extract a high enough amount of proteins, we lysed one T175-flask (Sarstedt, 833.912.002) per condition. 100% confluent MDCK cell monolayers residing on T175-flasks ($3.68x10^7$ cells per flask) were infected with 12 mL of *L.m.* bacterial suspension (more details in section "Bacterial infections of MDCK cells in monolayer") or not (uninfected controls). At 4 hpi *L.m.*-infected and control monolayers were either treated with 50 μM PD0325901 or vehicle control (DMSO). Lysis of L.m.-infected monolayers was performed either at 8 hpi or 24 hpi, while control uninfected monolayers were lysed and collected together with the 8 hpi infected sample.

For lysis, the cells were washed once with PBS, placed on ice, and immediately after, 1 mL lysis-buffer (4% w/v sodium dodecyl sulfate (SDS), in 100 mM tris(hydroxymethyl)aminomethane (Tris)/HCl, pH 8.0, 1:100 protease/phosphatase inhibitor cocktail (Cell signaling, #5872) was added. After 10 min, the cells were scraped with a cell scraper (Sigma, CLS3010-100EA) and transferred to a falcon tube. To degrade DNA and RNA, 0.5 μL/sample benzonase (Merck, 70746) was added to the samples, which were then vortexed, incubated at room temperature for 10 min, and transferred to screw cap microtubes (Sarstedt, 72.694.700) containing 500 μL glass beads (Roth, N033.1) for homogenization. The cells were homogenized at 6.5 m/s for 40 s twice by using a FastPrep-24 (MP Biomedicals) and incubated on ice for 2 min in between. Afterward, samples were centrifuged at the maximum speed 21300 x *g* for 1 min and the supernatant was collected. For reduction of cysteine disulfide bonds, 10 mM dithiothreitol (DTT, Roth, 6908.1) was added and samples were incubated at room temperature shaking (Thermomixer C, Eppendorf) for 45 min. For alkylation of cysteine thiol groups, 5.5 mM iodoacetamide (IAA, Sigma, I6125-10G) was added and samples were incubated in dark again at room temperature shaking for 45 min. Then, the suspensions were centrifuged at 12000 x *g* for 15 min. To precipitate the proteins, the supernatant was diluted 1:8 with ice-cold acetone/methanol mixture (8:1 v/v) and incubated overnight at −20°C. The next morning, the samples were centrifuged at 1000 x *g* for 5 min, followed by washing, resuspension of the protein pellet in 80% v/v acetone aq. and thoroughly vortexing. These steps were repeated two more times. The protein pellet was air dried for 10 min, rehydrated in 100 μL denaturation buffer (6 M urea, 2 M thiourea in 10 mM Tris/HCl, pH 8), and frozen at −80°C.

For the proteome analysis, for each experiment (MDCK monolayers infected for 8 h, 24 h and uninfected) mixtures with a ratio of 1:1 of samples treated with either 50 μM PD0325901 or DMSO (vehicle control) were prepared. This resulted in a total protein amount of 600 μg, of which one part was used for proteome analysis (10 μg). Dimethyl-labeling was performed[72] followed by label efficiency and label channel mixing checks in separate LC–MS/MS runs. Phosphopeptides were enriched using MagReSyn Ti-IMAC (titanium-immobilized metal affinity chromatography, ReSyn Bioscience) in two consecutive rounds of enrichment using total amount of 600 μg proteins per mix.[71]

The phosphoproteome and proteome of all samples were analyzed on an Q Exactive HF-X mass spectrometer (Thermo Fisher Scientific). An online-coupled Easy-nLC 1200 UHPLC (Thermo Fisher Scientific) was used to separate peptides on a 20 cm analytical column (75 μm ID PicoTip fused silica emitter) in-house packed with ReproSil-Pur C18-AQ 1.9 μm resin (Dr Maisch GmbH Ltd). Phosphopeptides and dimethyl-labeled proteomes were eluted using a 90 min and a 130 min gradient, respectively.

Raw files were processed with the MaxQuant software suite (Version 1.6.14.0).[55] MS/MS data were searched against UniProt *Canis lupus familiaris* (containing 43678 entries) and *L.m.* databases, containing commonly observed contaminants. The mass tolerance for precursor ions was set to 4.5 ppm and for fragment ions to 20 p.m. All search parameters were kept to default values except for the following: dimethylation for light (28.03 Da), intermediate (32.06 Da), and heavy (36.08 Da) labels was allowed on lysine residues and peptide N termini for phosphoproteome data. For all phospho raw files, phosphorylation on STY was defined as variable modification, while oxidation of methionine and protein N-terminal acetylation were set as variable modifications. Carbamidomethylation of cysteine residues was allowed as fixed modification. All searches were performed in trypsin/P-specific digestion mode. Data analyses were performed using Perseus software (Version 1.6.2.3)[56] to identify significantly changed phosphorylation sites (Threshold $p < 0.05$). The significantly changed phosphorylation sites that occurred in at least one replicate were analyzed with STRING software to perform functional enrichment analysis.[57] The resulting significant enriched GO subcellular localizations (Compartments) were visualized in a bubble plot using the R package ggplot2.[58]

Hybrid computational model to simulate infection *in silico*

A hybrid computational model was employed to simulate a two-dimensional (2-D) epithelial cell monolayer, integrating discrete and continuum modeling approaches, namely, an agent-based model (ABM) to simulate cells as individual entities and a finite element

model (FEM) to simulate the monolayer as a continuum.[73] Both techniques are integrated in an iterative loop, thus allowing the simulation of epithelial cells in monolayer over several time steps. In this framework, cell centroids are first represented as independent particles in the ABM, which are randomly distributed in the cell monolayer. Given the distribution of cells, we compute the balance of cell forces by assuming a quasistatic equilibrium and considering cell-cell interaction forces ($F_{ji}^{cell-cell}$). These forces depend on the distance between cell centroids, and we assume that when cells are in close proximity, they repel each other (contact inhibition), whereas two cells are pulled apart, there are attractive forces acting in both cells. This force-dependent behavior is assumed to follow the Lennard-Jones potential.[74] Additionally, we consider that cells are able to sense the stresses they are subjected to, responding in an active manner by generating additional loads (mechanosensing mechanism). This cell mechanical response entails cell actomyosin contraction and cell protrusion. Regarding the actomyosin contraction force (F_i^{contr}), we assume that the greater the tensile stress sensed by a given cell is, the more the cell contracts. Regarding the protrusion load (F_i^{protr}), it is assumed that the cell protrudes in the direction of lower tensile stress, which defines the direction of polarization of the cell. The magnitude of this force is proportional to the tensile stresses acting on the cell. Finally, it is assumed that surrounder cells proximal to the infection focus (proximal surrounders) exert forces pointing toward the infection focus ($F_{k,i}^s$), which reproduces the migration of surrounder uninfected cells during the mechanical competition that occurs during bacterial infection with *L.m.*

Cell centroids are then used to determine the Voronoi tessellation, which provides a distribution of cell polygons in the monolayer (polygons formed by the bisection of the connecting lines between neighboring points/cell centroids). It is assumed that each cell occupies the area of the polygon associated with its centroid. These polygons are discretised with triangles to generate a finite element mesh. Due to the geometrical properties of the cell (i.e., the thickness is much lower than the in-plane dimensions) we assume that the cell monolayer can be modeled in the FEM as a plane stress model. The cell monolayer is assumed to behave as a linear elastic isotropic material. We distinguish between infected and uninfected cells with varying elastic modulus (500 Pa for uninfected cells and 250 or 500 Pa for infected cells,[8] depending on the assumed scenario) and a Poisson's ratio of 0.49 for both of them. The forces computed in the ABM are then introduced in the FEM as concentrated forces in the cell centroids and in the vertices of the Voronoi polygons. To define the boundary conditions of the cell monolayer, we assume conditions of symmetry. The forces previously computed induce new deformations in the monolayer, which causes the movement of cells. The displacements of the cell centroids and the stress distribution inside each cell are used as new inputs for the ABM in the new iteration of the loop. This process is repeated until the end of the simulated period. The evolution of cell area, cell stresses and the displacements of the cells are then compared against experimental results. The ABM is implemented through custom made MATLAB files and the FEM is calculated with the commercial software ABAQUS CAE (Dassault systèmes Simulia Corporation).

QUANTIFICATION AND STATISTICAL ANALYSIS

We performed statistical analysis with Graphpad Prism 10 (Graphpad, RRID:SCR_002798). All box plots in the manuscript (unless otherwise indicated in the corresponding figure legends) show the following: horizontal line is the distribution's median, boxes indicate the 25% and 75% quartiles, whiskers indicate the 5 and 95% quantiles. Outliers are represented as dots unless the sample size is very high in which case they are not shown (that is the case only in Figures 2C–2F). The mean parameter values per independent recording are overlaid on the box plots and indicated with a circle (e.g., Figure 6C). Always at least three independent experiments are performed unless otherwise indicated. In the box plots showing cell stiffness measured via AFM (i.e., Figure 6F), the mean stiffness value is also superimposed on the box plots and indicated as dot. The figure legends indicate statistical test performed, *p*-values, and sample size. For comparison of two samples, we either used the non-parametric test Wilcoxon Rank-sum test (denoted as WRST) or the parametric Student's t-test (denoted as t test). To analyze more than two samples simultaneously, we first performed an ordinary one-way ANOVA to test whether there were significant differences among the samples ($p < 0.05$). If this was the case and the normality test was passed, we performed multiple comparisons using a Tukey test, comparing each column with the mean of every other column. The family-wise alpha threshold was 0.05 to get a 95% confidence interval.